DOI:
10.1038/s41586-019-0891-2

Document Version
Peer reviewed version

Published in final edited form as:
Nature. 2019 February 01; 566(7742): 126–130. doi:10.1038/s41586-019-0891-2.

Tissue curvature and apicobasal mechanical tension imbalance instruct cancer morphogenesis

Hendrik A. Messal[1,6], **Silvanus Alt**[2,3,6], **Rute M.M. Ferreira**[1,7], **Christopher Gribben**[1,7], **Victoria Min-Yi Wang**[1,7], **Corina Cotoi**[4], **Guillaume Salbreux**[2,*], **Axel Behrens**[1,5,*]

[1]Adult Stem Cell Laboratory, The Francis Crick Institute, 1 Midland Road, London NW1 1AT, UK

[2]Theoretical Physics of Biology Laboratory, The Francis Crick Institute, 1 Midland Road, London NW1 1AT, UK

[3]Max Delbrück Center for Molecular Medicine, Robert-Rössle Straße 10, 13125 Berlin, Germany

[4]Institute of Liver Studies, King's College Hospital, Denmark Hill, London SE5 9RS, UK

[5]King's College London, Faculty of Life Sciences and Medicine, Guy's Campus, London SE1 1UL, UK

Abstract

Tubular epithelia are a basic building block of organs and a common site of cancer occurrence[1–4]. During tumourigenesis, transformed cells overproliferate and epithelial architecture is disrupted. The biophysical parameters underlying the adoption of abnormal tumour tissue shapes are, however, not known. Here we show that the morphology of epithelial tumours is determined by the interplay of cytoskeletal changes in transformed cells and the existing tubular geometry. To analyse the morphological changes of tissue architecture during cancer initiation, we developed a three-dimensional (3D) whole organ imaging technique allowing tissue analysis at single cell resolution. Oncogenic transformation of pancreatic ducts led to two types of neoplastic growth: exophytic lesions expanding outwards from the duct, and endophytic lesions growing inwards to the ductal lumen. Myosin activity was higher apically than basally in wildtype cells but upon transformation, this gradient was lost in both lesion types. 3D vertex model simulations and a continuum theory of epithelial mechanics, incorporating the cytoskeletal changes observed in

[*]Corresponding authors: Dr Axel Behrens, Phone: +44 203 796 1194, Axel.Behrens@crick.ac.uk; Dr Guillaume Salbreux, Phone: +44 203 796 2009, Guillaume.Salbreux@crick.ac.uk.
[6]Co-first authors
[7]Co-second authors

Data availability. All relevant data and protocols are included within the paper, Extended Data and Supplementary Information. Source data for figures 1d,f; 2i-k,m; 3d; 4a,b,d; E1d,f; E2b; E5e; E6b-g,i-l; E7d,f,i,j,m,n; E8a-d,f,h; E10e,f are provided with this paper. The original datasets and resulting analyses, as well as methodological details are available from the corresponding authors upon reasonable request.

Code availability. 3D vertex model custom code is available upon request from S.A. (silvanus.alt@mdc-berlin.de).

Author contributions H.A.M., S.A., G.S. and A.B. conceived and designed the study. H.A.M. performed the experiments and analyses. C.G. and V.M-Y.W. helped with organoid experiments. S.A. performed and analyzed simulations and G.S. analyzed the continuum theory. R.M.M.F. assisted with study design and interpretation of data. C.C. assisted with lesion identification and description. G.S. and A.B. supervised the study. All authors discussed and interpreted the results and participated in writing the manuscript.

Author Information H.A.M and A.B. are inventors on a UK patent application (1818567.8) relating to a solution for the preparation of samples for 3D imaging.

Europe PMC Funders Author Manuscripts

transformed cells, indicated that the diameter of the source epithelium instructs the morphology of growing tumours. 3D imaging revealed that, in agreement with theory predictions, small pancreatic ducts produced exophytic growth, whereas large ducts deformed endophytically. Similar patterns of lesion growth were observed in tubular epithelia of the liver and lung, identifying tissue curvature and tension imbalance as fundamental determinants of epithelial tumourigenesis.

Mechanical alterations in cancer cells play an important role in tumourigenesis[5]. We addressed how mechanical alterations contribute to tumour formation in the context of an intact epithelium, using the pancreatic duct as a model. To preserve the geometric complexity of the adult pancreas, we developed a new technique for rapid whole-organ 3-dimensional immunostaining and imaging (FLASH, see methods) allowing robust quantitative assessment of organ architecture at the single-cell and tissue level. FLASH maintained pancreatic compartmentalisation and tissue integrity (Extended Data Fig.1a, b). We visualised the adult pancreatic ductal system by inducing expression of tdTomato in all duct cells (*R26-CAG-tdTomato; Hnf1b-CreERt2*). FLASH imaging of whole pancreata revealed an intricate hierarchy of tubules spanning the exocrine lobules (Fig. 1a, b, Extended Data Fig.1c, d and Supplementary Video 1). Ductal segments varied significantly in diameter (Fig. 1c, d), with smaller ducts composed of elongated cells and large ducts of cuboidal cells (Fig. 1, e, f). Confetti labelling showed clonal expansion predominantly along the cell elongation axis (Extended Data Fig.1e, f). These findings illuminate the complexity and heterogeneity of the pancreas ductal system (Fig. 1g).

To trigger epithelial deformations, we induced conditional mosaic activation of the KrasG12D oncogene with concomitant deletion of either p53 or Fbw7 tumour suppressors[1,2,6]. FLASH analysis of *KrasG12D; Fbw7 F/F; Ck19-CreERt* (KFCk19) and *KrasG12D; Fbw7 F/F; Hnf1β-CreERt* (KFH) mice revealed two morphologically distinct lesion types co-occurring in all pancreata analysed. Transformed ducts either evaginated basally, away from the duct lumen (designated “exophytic”), or invaginated apically, towards the duct lumen (designated “endophytic”) (Fig. 2a and Extended Data Fig. 2a-d). Exophytic lesions extended the duct lumen and formed globular structures (Fig. 2b, c, Extended Data Fig. 2e-g and Supplementary Video 2), which progressed to back-to-back gland-like ductal neoplasia (Fig. 2d). Endophytic lesions, in contrast, grew into the duct lumen in a papillary manner (Fig. 2e, f, Extended Data Fig. 2e and Supplementary Video 3), and progressed to intratubular neoplasia with local obstruction of the duct lumen (Fig. 2g). Activation of KrasG12D and deletion of Fbw7 or p53 in acinar cells, located at the tips of small calibre ducts, induced acinar-to-ductal metaplasia (ADM), leading to Krt19-positive globular lesions continuous with the ductal tree (Extended Data Fig. 3a-h and Supplementary Videos 4-5). In mice with duct-specific (KPCk19) or pancreas-wide (KPC) KrasG12D activation and p53 deletion[1,2,7], we also identified exophytic and endophytic lesions, indicating that these observations are not dependent on a particular oncogene combination (Extended Data Fig. 4a-e). Lesions with endophytic and exophytic morphology were also observed in the pancreatic tissue of pancreatic ductal adenocarcinoma (PDAC) patients (Extended Data Fig. 4f).

Pancreatic cancer cells co-opt pancreatic stellate cells as cancer associated fibroblasts (CAFs), which support tumour invasion and metastasis[8,9]. Both murine and human exophytic lesions, which invade the surrounding parenchyma, recruited CAFs more efficiently than endophytic lesions that grow into the duct lumen, although both lesion types showed rapid proliferation (Extended Data Fig. 5a-c). Advanced exophytic lesions displayed more epithelial-to-mesenchymal transition as judged by the numbers of tumour-traced mesenchymal cells (Extended Data Fig. 5d, e). Thus, exophytic growth fosters more aggressive lesion development.

Because tissue morphology depends on cellular tension and contractility, driven by the actomyosin cortex[10], we quantified the distribution of the key cortex components F-actin and pMLC2[11–13] in single cells in KFCk19 and KPC mice, shortly after oncogene activation and before the occurrence of neoplastic lesions. F-actin and pMLC2 staining intensity was significantly higher apically than basally in wildtype cells. Upon transformation, this gradient was strongly reduced (Fig. 2h-k and Extended Data Fig. 6a-h). Acinar-derived lesions, which show redistributed F-actin[14,15] displayed a similar apical-basal pMLC2 shift (Extended Data Fig. 6i, j), supporting a cell-type-independent effect of transformation. Phosphorylated focal adhesion kinase (pFAK) and vinculin (VNC), redistributed in the same manner, and the integrins ItgA2, ItgA6 and ItgB1[16] were overexpressed basally (Extended Data Fig. 6k, l). When cultured *in vitro* as organoids, pancreatic cells from KPC mice displayed similar disruptions of the pMLC2 gradient (Fig. 2l, m).

We then investigated possible molecular mechanisms behind pMLC2 perturbation in transformed cells. Phosphatase inhibition in wildtype organoids abolished the basal-apical pMLC2 gradient, suggesting that phosphatase activity contributes to pMLC2 polarisation (Extended Data Fig. 7a-d). Disruption of apical-basal polarisation has been reported in Ras transformed cells and oncogenic Kras signalling stimulates pMLC2[17,18]. The MEK1/2 target ERK regulates actin polymerisation[19] and activates myosin light chain kinase (MLCK) which phosphorylates MLC2[20,21]. We found that *KrasG12D; Pdx1-Cre* (KC) mice contained ductal structures with equal apical-basal pMLC2 distribution in line with the observed F-actin distribution in KC mice[14] (Extended Data Fig. 7e, f). Furthermore, apical pMLC2 accumulation could be partially restored by MEK1/2 inhibition in KPC organoids. Overall these results identify oncogenic Kras-MEK-ERK hyperactivation as a driver of pMLC2 shift, possibly by overriding phosphatase activity (Fig. 2n and Extended Data Fig. 7g-j). In contrast, ROCK inhibition led to an overall reduction of pMLC2 without affecting its relative distribution (Extended Data Fig. 7k-n).

To test whether the pMLC2 perturbation in transformed cells could explain the observed lesion deformation, we developed a computational model of the pancreatic duct using a 3D vertex model simulation framework integrating duct cell geometry, apical, basal and lateral surface tensions, and cell volume conservation (Fig. 3a)[22,23]. We assumed that apical and basal surface tensions in wildtype and transformed cells were proportional to the relative fluorescence intensities of pMLC2[11,12,24] (Fig. 3b and Supplementary Modelling Procedures). To mimic oncogenic transformation, we introduced a single cell with modified surface tensions in accordance with averaged pMLC2 fluorescence intensity changes observed experimentally (Fig. 2j) and simulated successive rounds of cell division (Fig. 3b)

to match cell counts observed at different time points. Simulations were performed for tubes of different diameters by varying the number of circumferential cells (Extended Data Fig. 8a). Strikingly, without further fitting, we found evaginating and invaginating deformations which closely resembled those observed in the pancreas (Fig. 3c). Furthermore, simulations showed a transition from evaginating deformations in small ducts to invaginating deformations in large ducts at ~17 μm diameter (Fig. 3d and Extended Data Fig. 8b). In simulations where only cellular proliferation was considered, without changes in surface tension of the transformed cells, deformations were exophytic and no transition was observed (Extended Data Fig. 8c).

To assess whether lesion shape correlated with ductal diameter *in vivo*, we measured the radial deformation of transformed pancreatic ducts of KFCk19 mice throughout the ductal tree. Strikingly, transformed ducts with a diameter less than 17 μm deformed exophytically, while those with a diameter greater than 17 μm deformed endophytically, in agreement with the model predictions (Fig. 3d and Extended Data Fig. 8d). These observations, together with our computational model, strongly suggested that ductal deformations are dependent on duct diameter.

To confirm our computational prediction that hyperproliferation alone without mechanical changes is insufficient to induce endophytic lesion formation (Extended Data Fig. 8c), we used *Fbw7 F/F; Krt19-creERt* (FCk19) mice where *Fbw7* inactivation induces hyperproliferation of duct cells without leading to oncogenic transformation[2,25]. *Fbw7 F/F* duct cells had no alterations in pMLC2 intensity or integrin levels compared with wildtype cells (Fig. 4a and Extended Data Fig. 8e-h). FLASH imaging identified local duct cell crowding and a mild expansion of the duct lumen without neoplastic deformations (Fig. 4b, c). These findings support our model predictions that hyperproliferation alone cannot account for diameter-dependent exophytic versus endophytic lesion formation and that only endophytic lesion growth requires altered apicobasal tension.

To determine whether cytoskeletal alterations could distinguish between hyperproliferative benign and malignant ductal reactions, we compared cellular pMLC2 localisation and Itga2 expression in caerulein-induced pancreatitis[26], genetic hyperproliferation of FCk19 mice and early neoplastic lesions of KPC mice. Whilst apically depleted in transformed duct cells, pMLC2 was maintained in reactive and hyperproliferative ducts (Extended Data Fig. 9a-c). ItgA2 was strongly expressed in transformed lesions but not in reactive or hyperproliferative ducts (Extended Data Fig. 9d). Thus, cytoskeletal redistribution distinguishes oncogene-induced ductal transformation from benign hyperproliferation.

In order to test our hypothesis that ductal deformation is dependent on duct diameter, we developed a continuum theory of a circular epithelium subjected to asymmetric apico-basal surface tension[27–29] (Supplementary Modelling Procedures and Extended Data Fig. 10a). We considered the deformation induced by a localised patch of transformed epithelium. Reflecting the cytoskeletal changes in transformed cells, we assumed that the patch had increased basal and decreased apical tension, leading to a preferred inward curvature of the transformed tissue (Extended Data Fig. 10b). In small tubes, this tension imbalance is not large enough to overcome the resistance of the surrounding epithelium, and the lesion grows

outwards in an exophytic manner (Extended Data Fig. 10c, left). In large tubes, early tumours are more free to adopt their preferred invaginating shape, and the lesion grows inward (Extended Data Fig. 10c, right). Our generic continuum model therefore predicts a transition from exophytic to endophytic lesion at a threshold tube radius that depends on the tissue bending modulus and the magnitude of apico-basal tension changes in the transformed region (Extended Data Fig. 10d).

The simplicity of the continuum model suggested that the dependency of lesion shape on ductal diameter was a universal principle. Keratin 19 is a general marker of ductal epithelia[30], and in KFCk19 mice in addition to pancreatic cancer we observed neoplastic lesions resembling squamous cell carcinoma precursors in the airways of the lung, and biliary neoplasia in the intrahepatic biliary tree. In both organs, transformed cells showed apical-basal redistribution of pMLC2, indicating that oncogenic Kras-driven cytoskeletal disruption is tissue independent (Extended Data Fig. 10e, f). The hepatic ductal system comprised both small and large ducts that gave rise to exophytic or endophytic lesions, respectively. The bronchiolar tree of the lung, however, is built of airways with diameters only above 30 μm, which gave rise to endophytic neoplasia only (Fig. 4d-f). Thus, remarkably, a tube diameter of ~20 μm appears to be the threshold for the transition from exophytic to endophytic tumours during lesion initiation in different organs and cancers (Fig. 4g). Together, our findings indicate that the local curvature of the source epithelium, together with mechanical changes within the transformed cells, instructs the direction of epithelial deformation and ultimately directs tumour morphology.

Online-Only Methods

Mice

All experiments were approved by the London Research Institute Animal Ethics Committee or the Animal Welfare and Ethical Review Body of the Francis Crick Institute and conformed to UK Home Office regulations under the Animals (Scientific Procedures) Act 1986 including Amendment Regulations 2012. Tumour experiments are permitted until mice experience excessive weight loss or display overt signs of illness. In no experiments were permitted endpoints exceeded, all mice were humanely killed and analysed at the onset of transformation before macroscopic tumour development. No longitudinal tumour measurements were performed as this was technically not feasible for microscopic lesions.

Ela1-CreERT2[31], Krt19-CreERT[30], Hnf1β-CreERT2[32], Pdx1-Cre[33], Ptf1a-CreERT[34], LSL-Kras G12D/wt[35], Fbw7 F/F[36], MIP-GFP[37], p53 F/F[38], Rosa26-Confetti[39], Rosa26-CAG-tdTomato[40] and Rosa26-LSL-YFP[41] mouse lines have been previously described. Mice were genotyped using Transnetyx Inc. and intercrossed to yield the desired genotypes. For Cre recombinase activation adult mice received daily intraperitoneal injections of tamoxifen (Sigma-Aldrich) in peanut oil (Sigma-Aldrich) at a dose of 100 mg/kg bodyweight as follows: Rosa26-CAG-tdTomato; Hnf1β-CreERT2 mice received 5 injections, Rosa26-Confetti; Hnf1β-CreERT2 mice received 2 injections, Krt19-CreERT mice received 2 injections. Mice were analyzed 7 days, 10 days or 3 weeks after the last tamoxifen injection before macroscopic tumours were apparent. Ela1-CreERT2 and Ptf1a-CreERT mice received 5 tamoxifen injections. To induce acute pancreatitis, mice were subjected to a short caerulein

treatment. Mice received intraperitoneal injections of caerulein (Sigma-Aldrich) in PBS at a dose of 50 μg/kg bodyweight (7 times a day, at hourly intervals, for 2 days). Ela1-CreERT2 and Ptf1a-CreERT mice were analysed after 2 to 5 months to study transformation. Wildtype mice were analyzed 4 days after Caerulein to assess acute pancreatitis.

In-situ retrograde pancreas ductal perfusion

Mice were euthanized by cervical dislocation and under a stereo microscope, the abdominal wall and peritoneum were opened and the pancreatic head located. A suture was placed around the first bifurcation of the extrahepatic biliary tree. With an insulin gauge, 50 μl of 12 mg/ml FITC-conjugated dextran (Sigma-Aldrich; average mol wt 2,000,000) were injected into the hepato-pancreatic duct by cannulation of the duct through the duodenal papilla.

FLASH

FLASH was developed for the rapid detection of a multitude of antigens in intact adult organs by mild non-destructive epitope recovery (FLASH – Fast Lightmicroscopic analysis of Antibody-Stained wHole organs). Mice were euthanized by cervical dislocation. Cardiac perfusion was carried out with 20 ml PBS. Pancreata were removed attached to spleen and duodenum without perturbing the gland. Samples were fixed in 4% PFA overnight at 4°C. Specimens were washed in PBT (0.4% Triton X-100 (Sigma-Aldrich) in PBS) twice for one hour and incubated in 200 mM boric acid (Sigma-Aldrich) with 4% SDS (Sigma-Aldrich) pH 7.0 overnight at 54°C. Samples were washed in PBT for three hours with three volume exchanges. For immunolabelling, samples were incubated in FLASH blocking buffer (1% bovine serum albumin (Sigma-Aldrich), 5% DMSO (Sigma-Aldrich), 10% fetal calf serum (Gibco), 0.02% sodium azide (Sigma-Aldrich), 0.2% Triton X-100 in PBS) for one hour and incubated with antisera (all 1:100) for at least 16 hours at room temperature on a nutator. Samples were washed by three volume exchanges PBS and incubated with secondary antibodies (all 1:100) for at least two days at room temperature. Samples were washed by three volume exchanges with PBS and gradually dehydrated in 30%, 50%, 75%, 2x 100% MetOH (Sigma-Aldrich), 1hr each and, in a glass dish, immersed in methyl salicylate diluted in MetOH: 25%, 50%, 75%, 2x 100% methyl salicylate (Sigma-Aldrich), 30 min each, protected from light.

Fluorescent proteins were stained by immunofluorescence. The following antibodies were used: Amylase (goat, SCBT), GFP (goat, Abcam), GFP (mouse, Roche), Krt19 TROMA III (rat, DSHB), Tomato (rabbit, Rockland). All secondary antibodies were Alexa-dye conjugates (ThermoFisher). Nuclei were stained with DRAQ5 (Biostatus).

3D imaging

Organs were imaged on a Zeiss LSM 780 confocal microscope equipped with a 405 nm laser, an argon laser, a DPSS 561 nm laser, a HeNe 594 nm laser and a HeNe 633 nm laser using the following objective lenses: 10x/0.45 Ph2 Plan-Apochromat and 25x/0.8 LD LCI Plan-Apochromat. Since the limited working distance of the objectives did not allow to image throughout the total thickness of the liver, liver lobes were bisected prior to imaging. 3D Image analysis and quantifications were performed using Imaris software (Bitplane). For

Europe PMC Funders Author Manuscripts

display purposes, 3D images were gamma corrected and clipping planes were used to crop data sets to the relevant areas. Scale bars refer to the centre of the 3D view.

3D quantifications of ductal and cellular geometry

Cell height, length and duct diameter were measured using Imaris software. Stainings for Krt19 were used to demark the duct cell shape, and length and height were measured for individual cells using the measurement tool in optical sections. Five cells were measured per duct. The cell width was calculated using the quantifications of duct diameter and number of circumscribing cells. The duct diameter was measured in optical sections as the distance of opposing duct walls in one optical section (xy plane) and perpendicular to it (z), and for each duct, the average of both values was calculated. The number of duct circumscribing cells was counted manually using 3D representation and optical sections.

Quantification of the relative division plane

Rosa26-Confetti; Hnf1β-CreERT2 mice received 2 intraperitoneal tamoxifen injections at a dose of 100 mg/kg bodyweight, which induced recombination and fluorescent protein expression in less than 1% of duct cells as estimated from 3D imaging data. Clones were identified as clusters of directly adjacent cells that had the same fluorescence and subcellular fluorescent protein localization, and were surrounded by non-recombined cells. Using Imaris software, a surface describing the clone was automatically reconstructed in the channel of the fluorescent protein and split manually into surfaces describing each cell. Measurement points were positioned automatically into the center of each surface (clone cell) and into the center of the ductal lumen on both sides of the clone. The cell division direction was determined automatically as the angle between the line connecting the cell surface centers and the line connecting the two measurement points in the ductal center.

Histopathology, immunohistochemistry and immunofluorescence

Histological and immunohistochemical analyses were performed as previously described[2]. The following antibodies were used: Cdh1 (rat, Novex), Cortactin (rabbit, Abcam), GFP (goat, Abcam), GFP (mouse, Roche), ItgA2 (rabbit, Abcam), ItgA6 (rabbit, Abcam), ItgB1 (rabbit, Abcam), Ki67 (rat, Biolegend), Krt19 TROMA-III (rat, DSHB), MLC2 pSer19 (rabbit, NEB), Myosin (rabbit, Abcam), Nestin (mouse, BD transduction), Pdgfrβ (rabbit, NEB), PTK2 pTyr397 (rabbit, ThermoFisher), SMA (mouse, Agilent), SMA (mouse, Sigma), Tomato (rabbit, Rockland), Tomato (goat, Biorbyt), Vimentin (rabbit, NEB), Vinculin (mouse, Sigma-Aldrich). DBA-rhodamine and DBA-FITC were from Vectorlabs. F-actin was stained with Phalloidin-TRITC (Sigma-Aldrich) and nuclei with DAPI (Sigma-Aldrich). F-actin staining of LSL-KrasG12D; p53 F/F; Pdx1-Cre pancreata and wildtype littermate control pancreata was performed on cryosections. Samples were embedded fresh in OCT medium and after sectioning fixed in 5% NBF for 10 min. Slides were washed in 0.2% Triton X-100 in PBS for 10 min and incubated in FLASH blocking buffer for 30 min. Staining reagent incubations were performed as above. Fluorescent stainings were imaged on a Zeiss LSM 780 confocal microscope. Chromogenic DAB stainings were imaged on a Zeiss Axio Scan Z1 Slide Scanner.

Quantification of staining intensities of actomyosin cortex components

Immunofluorescence was performed as detailed above and imaged by confocal microscopy with a 40x/1.3 Plan-Apochromat oil immersion lens and two-to-fourfold optical zoom or with a 63x/1.46 Alpha Plan-Apochromat oil immersion objective. Lesions were classified as endophytic or exophytic based on recombination status and morphological presentation. At early stages (10 days after recombination), some recombined non-transformed cells may have been included in the transformed classification, but at later stages transformed and non-transformed cells could be classified unambiguously. Per lesion one optical section was analyzed by intensity quantification of transformed cells and neighbouring wildtype cells using ImageJ software (NIH). Images were converted into composite images where green and red marked Cdh1 (E-cadherin, to identify lateral membrane) and GFP (to identify genetically recombined cells), respectively, and the blue channel depicted the staining to be quantified. In each image, transformed cells were distinguished from wildtype by GFP positivity and all cells with clear lateral Cdh1 staining were included in intensity measurements. Cells with apical or basal Cdh1 positivity were omitted from analysis as such signal could be an artefact from lateral surfaces of diagonally cut cells in front or behind the cell of interest. Thus, only cells cut through the middle were analyzed. Basal-apical intensity gradients were quantified for each cell. Pixel intensities of the blue channel along a straight line from basal to apical edge, equidistant from the two Cdh1 stained lateral cell edges, were recorded. To control for differences in cell height and overall staining intensity, the profiles were aligned for cell height by equally distributing values along the profile of the tallest cell without filling the resulting gaps, and normalized for intensity by subtracting the minimum value from each intensity profile and dividing by its average value. For comparison, normalization to nuclear levels was carried out and the localization of intensity peaks was similar in both methods.

For integrin quantifications, intensities were measured along the basal edges of transformed and neighbouring wildtype cells. Freehand lines were drawn between the Cdh1 stained lateral surfaces without crossing the Cdh1 signal to avoid carry-over from the lateral cortex. For each measured cell an additional intensity measurement was taken from the inner nuclear region. To account for overall differences in staining intensities between images, the nuclear intensity was used as background value for normalization per cell.

Human samples

Human pancreatic tissue sections were obtained from King’s College Hospital patients (n=4) undergoing surgery for pancreatic neoplasia, who kindly consented to donate their samples for research. Sections were stained with haematoxylin and eosin, or antibodies for SMA or Pdgfrβ and histopathologically examined. The collection of samples was approved by the NHS Health Research Authority following assessment by a Research Ethics Committee (HSC REC B; reference 16/NI/0119).

Organoid culture

Pancreata were dissected and placed into ice-cold advanced DMEM/F-12 with 50 U/mL penicillin-streptomycin (ThermoFisher). Tissue was minced on ice and incubated in 1 mg/mL collagenase V (Sigma-Aldrich) in DMEM/F-12 for 40 min at 37°C. Digestion was

stopped by addition of ice-cold advanced DMEM/F-12 and cells collected by centrifugation (300 g, 5 min at 4°C). Samples were further digested with trypsin for 5 min at room temperature and the reaction was stopped with ice-cold 2 % FCS in PBS. The suspension was filtered through a 70 μm nylon mesh, and after centrifugation cells were plated in Matrigel. Organoid media was used as previously described[42,43]. Organoids were passaged once a week 1:10 using non-enzymatic TrypLE (ThermoFisher). For pharmacological inhibition of MEK1/2 or ROCK activity, KPC organoids were incubated with 8 μM U0126 (Promega) in DMSO or 5 μM H1152 (Tocris) in DMSO or, as control, with an equivalent volume of DMSO in organoid media for 16 hrs. For phosphatase inhibition, wildtype organoids were incubated with 2 μM okadaic acid (Tocris) in DMSO or 5 μM tautomycetin (Tocris) in DMSO or equivalent volume of DMSO (control) in organoid media for 1 hr. Experiments were carried out in triplicate for six independent organoid lines established from three wildtype mice and three LSL-KrasG12D; p53 F/F; Pdx1-Cre mice as indicated in the figure legends. Experiments were performed triple-blinded with one operator preparing the cells, a second operator adding drugs and a third operator staining and quantifying pMLC2 distribution.

Organoid staining

For staining, organoids were cultured in 8-well glass-bottom dishes (Ibidi). Organoids were washed in PBS for 5 min and fixed in 5% NBF in 0.1% Triton X-100 in PBS for 15 min at room temperature. Cells were washed with 0.2% Triton X-100 in PBS for 30 min and incubated in FLASH blocking buffer for 1 hr. Primary and secondary antibody incubations were extended overnight at 4°C with 1 hr washes in PBS after each incubation. For imaging, wells were immersed in fluorescence mounting medium (Dako). Images were taken on a Zeiss LSM 780 confocal microscope as described above (3D imaging).

Statistics

For experimental data, statistical significance was calculated using the Mann-Whitney Test (two-tailed, non-parametric, for unpaired samples) with *P*-values as indicated in the figure legend.

Extended Data

Europe PMC Funders Author Manuscripts

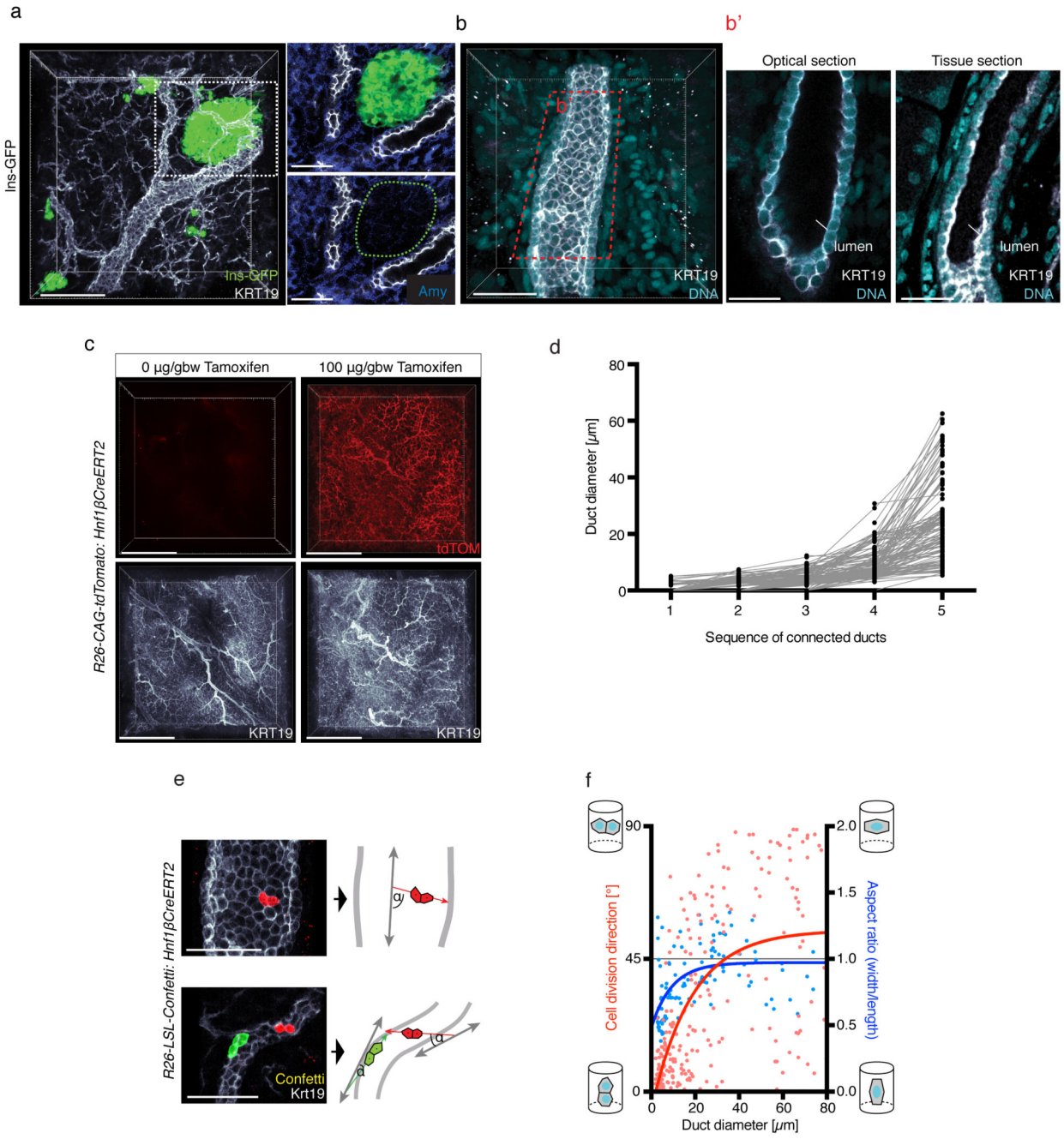

Extended Data Figure 1. Preserved organ integrity after FLASH.

(a) FLASH staining of an insulin(Ins)-GFP reporter mouse for amylase (Amy), Krt19 and Ins-GFP. Left, 3D reconstruction demonstrating complex organisation of islets and pancreatic ducts. Scale bar 100 µm. Right, optical section through the indicated area (left) showing preserved compartmentalisation into exocrine and endocrine glands as seen by the mutually exclusive staining for Amy, Krt19 and Ins-GFP. Scale bars 50 µm. Representative of 5 mice. **(b)** 3D view of a high-caliber duct (32 µm diameter) stained for Krt19 and DNA, demonstrating preserved epithelial integrity. Scale bar 50 µm. **(b')** Left, optical section

through the indicated area in (b) demonstrating the continuous duct cell monolayer and preserved duct lumen. Scale bar 30 μm. Representative of 6 mice. Right, staining for Krt19 and DNA on a 4 μm tissue section of paraffin-embedded pancreas. Scale bar 30 μm. **(c)** FLASH staining for tdTomato (tdTOM) and Krt19 on pancreata of *R26-CAG-tdTomato; Hnf1βCreERT2* mice without (left) and with (right) intraperitoneal injection of 100 μg tamoxifen per gram bodyweight. Scale bars 500 μm. Representative of 3 mice. **(d)** Arborisation of the ductal tree. Each dot represents one duct and lines indicate ramification. For three Krt19 stained pancreata, z-stacks of at least 30 random high-magnification views were taken. Per view the largest duct was identified and diameters were measured for four subsequent branching ducts to categorise the mode of arborisation. For ducts with more than one furcation, the sequence was continued with the biggest duct ramifying from it. Terminal duct cells were assigned a duct diameter of 0 μm to indicate ending of the ductal tree. **(e)** Cell division direction was measured on two-cell clones from tamoxifen-treated *R26-LSL-Confetti; Hnf1β-CreERt2* mice as the angle determined with respect to the line connecting both nuclei and the directionality of the duct. (n=263 clones, 5 mice). **(f)** Cell division direction and cell aspect ratio in ducts of varying diameter. Solid lines represent exponential fits. Cell division, n=263 clones, 5 mice; aspect ratio, n=120 ducts, 7 mice.

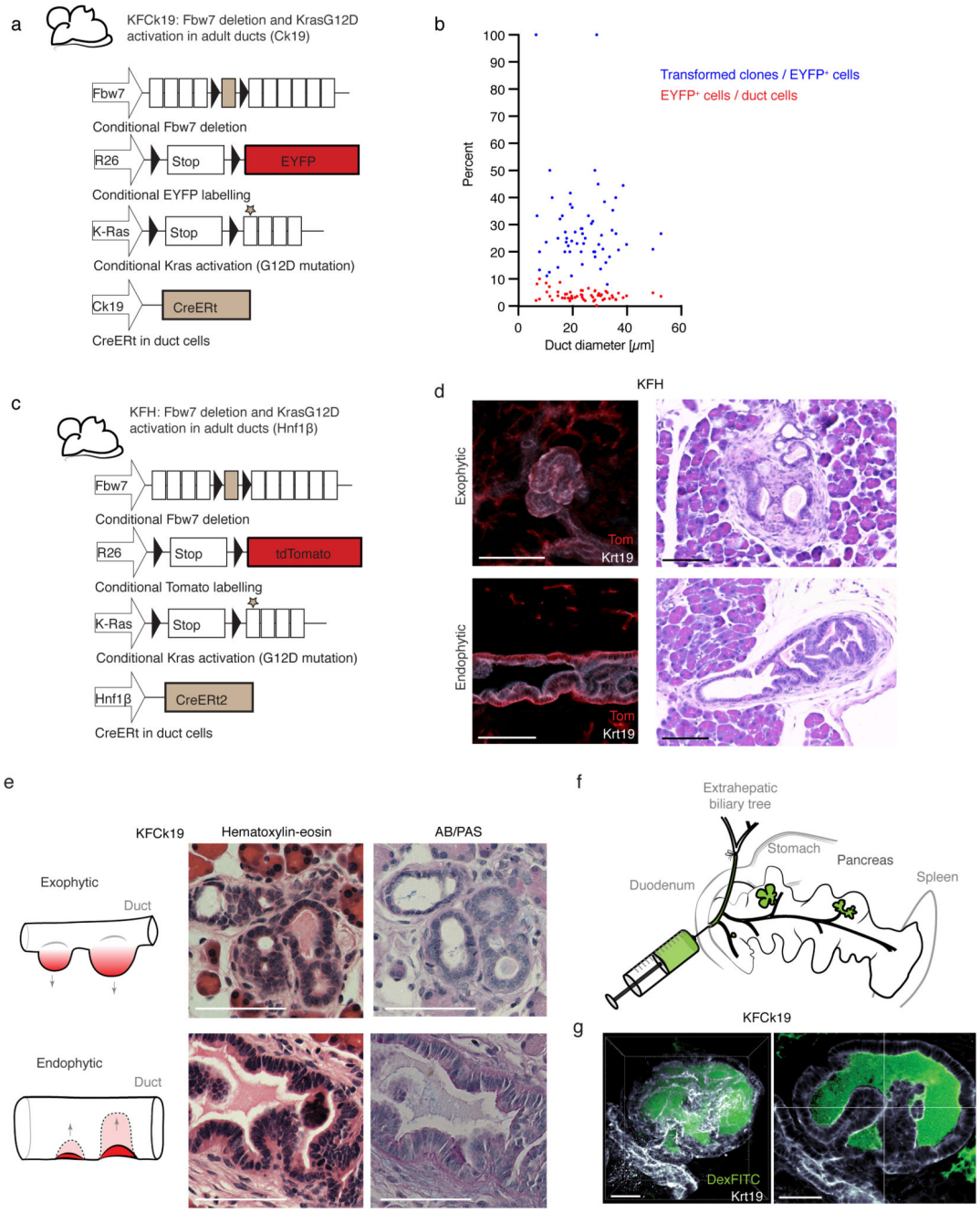

Extended Data Figure 2. Exophytic and endophytic neoplasia in *KrasG12D; Fbw7 F/F* model.

(a) KFCk19 mouse model for tumor induction in the ductal epithelium triggered by *Fbw7* exon deletion and *KrasG12D* activation. **(b)** Recombination efficiency of low-dose tamoxifen injection and number of transformed clones per number of recombined cells per duct were quantified one week after tamoxifen injection in KFCk19 mice. EYFP-traced Krt19^{+} cells were quantified per duct and total number of duct cells estimated by dividing the duct length by the average cell length measured for this duct and multiplying this by the average number of circumscribing cells for this duct. Transformed clones were recognised as

groups of more than three EYFP-traced cells sharing an interface. 1 dot represents one duct (112 ducts, 3 mice). **(c-d)** KFH mouse model for alternative targeting of pancreatic ducts. **(d)** Left, 3D rendering of exophytic neoplasia (top) and endophytic neoplasia (bottom) of KFH mice. Staining for Krt19 and tdTomato. Scale bars 100 μm. Right, H&E stainings for KFH exophytic (top) and endophytic (bottom) lesions. Scale bars 100 μm. Representative of 4 mice. **(e)** H&E and AB/PAS staining for exophytic and endophytic lesions in KFCk19 mice demonstrating non-mucinous character typical of duct-derived neoplasia[2]. Scale bars 100 μm. Representative of 3 mice. **(f)** Experimental strategy for visualizing the connection of exophytic neoplasia with the ductal tree. The extrahepatic bile duct was cannulated at the ampulla and the pancreas ductal tree perfused with 50 μl FITC-labelled dextran. **(g)** DexFITC uptake by an exophytic KFCk19 lesion demonstrating lesion connection to the ductal system. Left, 3D view and right, optical section. Scale bars 50 μm. Representative of 4 mice.

Europe PMC Funders Author Manuscripts

Europe PMC Funders Author Manuscripts

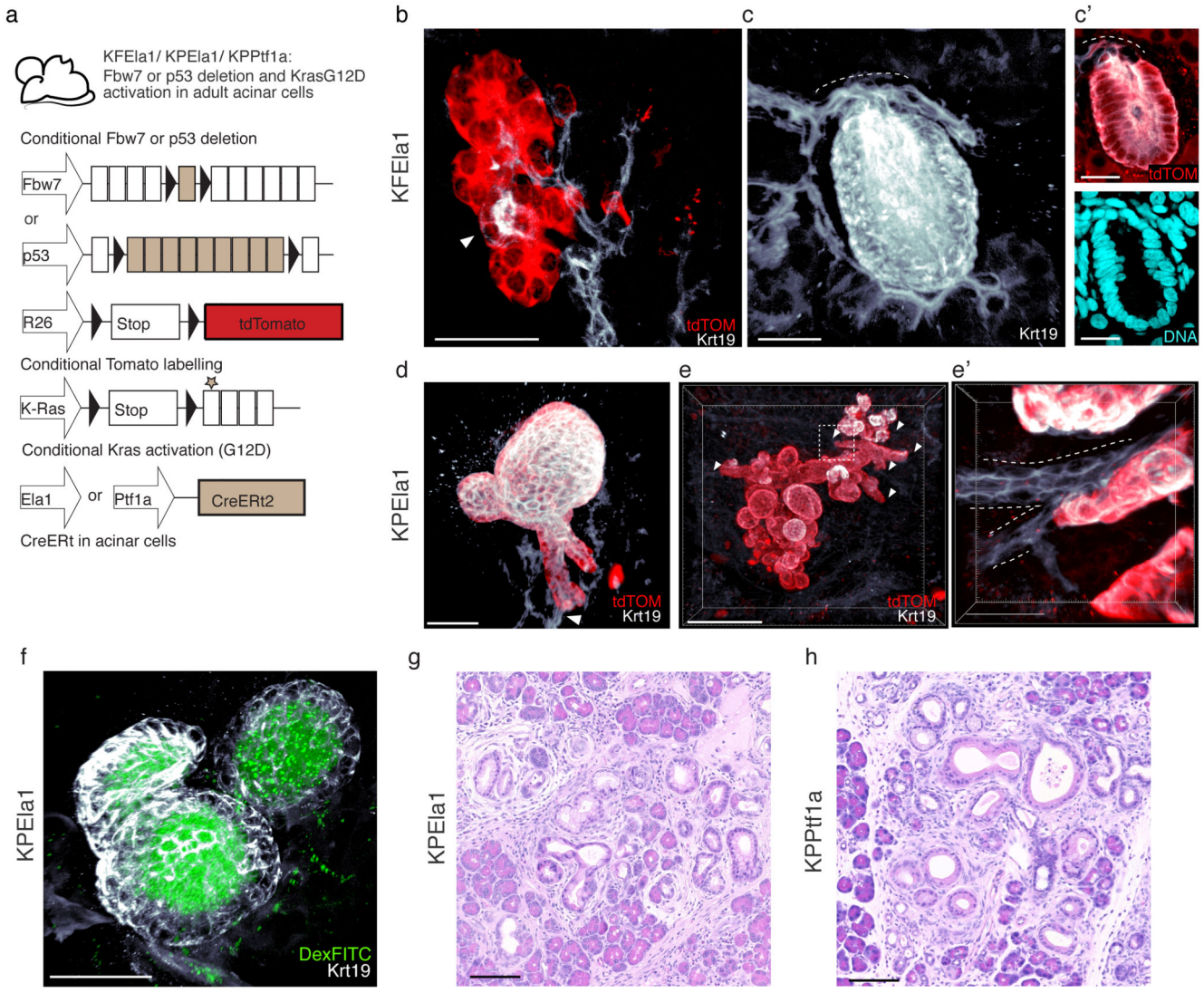

Extended Data Figure 3. Morphology progression of acinar-derived neoplasia.

(a) Schematic illustrating genetic strategy for acinar cell transformation by *KrasG12D* activation with concomitant *P53 F/F* or *Fbw7 F/F* deletion using Ela1-CreERt or Ptf1a-ERt2 drivers. **(b-c)** *KrasG12D; Fbw7 F/F; Ela1-CreERt* mice (KFEla1). **(b)** 3D view of acinar-to-ductal metaplasia as identified by local upregulation of Krt19 expression in acinar cells. Shown are td-Tomato-traced acini connected to a terminal duct. Arrow head demarcates Krt19 expression by the middle acinus, forming a small ring of acinar-derived, td-Tomato-traced Krt19^{+} cells. Scale bar 50 μm. Representative of 3 mice. **(c)** 3D projection of a globular KFEla1 lesion in contact with a small-calibre duct (dotted line). Scale bar 20 μm. **(c')** Optical sections of the lesion shown in (c) demonstrating td-Tomato tracing (top) and globular morphology (bottom). Scale bars 20 μm. Representative of 3 mice. **(d-g)** *KrasG12D; p53 F/F; Ela1-CreERt* mice (KPEla1). **(d)** 3D view of a globular td-Tomato-traced KPEla1 lesion connected to a terminal duct (arrow head). Scale bar 50 μm. Representative of 4 mice. **(e)** 3D projection of a large KPEla1 lesion showing central grape-

Europe PMC Funders Author Manuscripts

like morphology of back-to-back globular structures and maintained connection to several small caliber ducts (arrowheads) at the lesion edge. Scale bar 200 μm. **(e')** Higher magnification of area indicated in (e) demonstrating seamless connection of acinar-derived $Krt19^{+}$ cells and wildtype ductal epithelium (dotted lines). Scale bar 30 μm. Representative of 4 mice. **(f)** Retrograde perfusion of the ductal tree with dextran-FITC as in Extended Data Fig. 2f demonstrating direct connection of acinar-derived lesions to the ductal system. 3D view of a KPEla1 lesion. Scale bar 50 μm. Representative of 3 mice. **(g)** H&E staining of a KPEla1 lesion demonstrating globular morphology. Scale bar 100 μm. Representative of 6 mice. **(h)** *KrasG12D; p53 F/F; Ptf1a-CreERt2* (KPPtf1a) mice. H&E staining demonstrating globular morphology of lesions. Scale bar 100 μm. Representative of 5 mice.

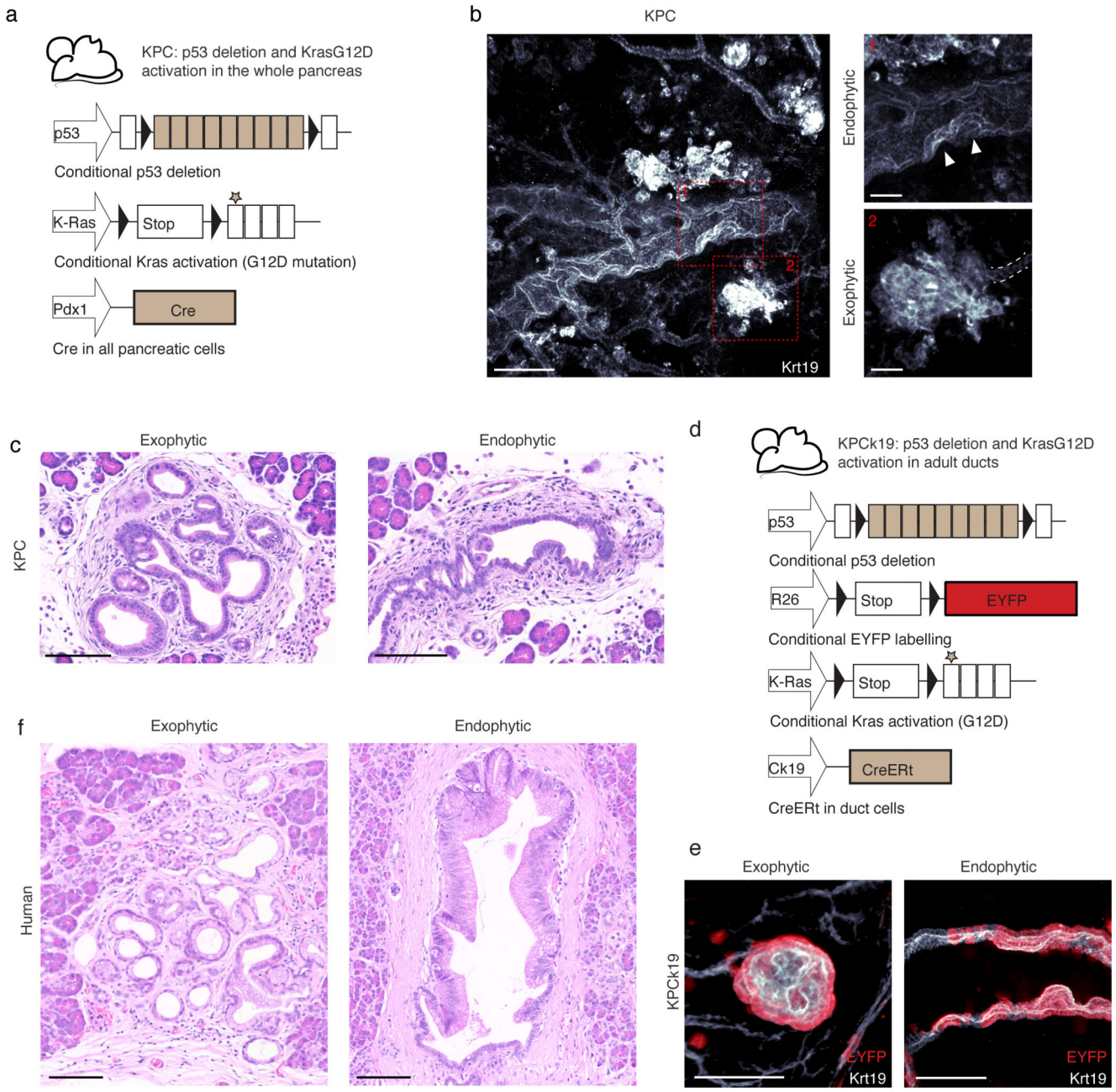

Extended Data Figure 4. Exophytic and endophytic neoplasia in *KrasG12D; p53 F/F* models and in human pancreas.

(a-c) Endophytic and exophytic lesions induced by *p53* deletion with *KrasG12D* activation upon Pdx1-Cre-induced whole-pancreatic recombination (KPC). **(b)** 3D view of a pancreatic region of a 3-week old mouse with endophytic (1) and exophytic (2) deformations. Scale bar 150 μm. **(1-2)** Higher magnifications of the indicated areas in (b). Scale bars 50 μm. **(1)** Arrowheads demarcate invaginations typical of endophytic growth. **(2)** Dotted line marks a morphologically normal small-calibre duct in contact with a globular, exophytic lesion. Representative of 6 mice. **(c)** Hematoxylin-eosin (H&E) staining for exophytic (left) and

Europe PMC Funders Author Manuscripts

endophytic (right) lesions in the KPC model. Scale bars 100 μm. Representative of 6 mice. **(d-e)** Exophytic and endophytic lesions induced by *p53* deletion with *KrasG12D* activation in pancreatic ducts (Ck19-CreERt; KPCk19). **(e)** 3D projection of exophytic (left) and endophytic (right) lesion shapes in KPCk19 mice. Scale bars 100 μm. Representative of 3 mice. **(f)** H&E staining of tissue sections from background pancreas of a patient presenting with pancreatic ductal adenocarcinoma. (Left) Exophytic lesion. (Right) Endophytic lesion. Scale bars 100 μm. 4 patients.

Europe PMC Funders Author Manuscripts

Europe PMC Funders Author Manuscripts

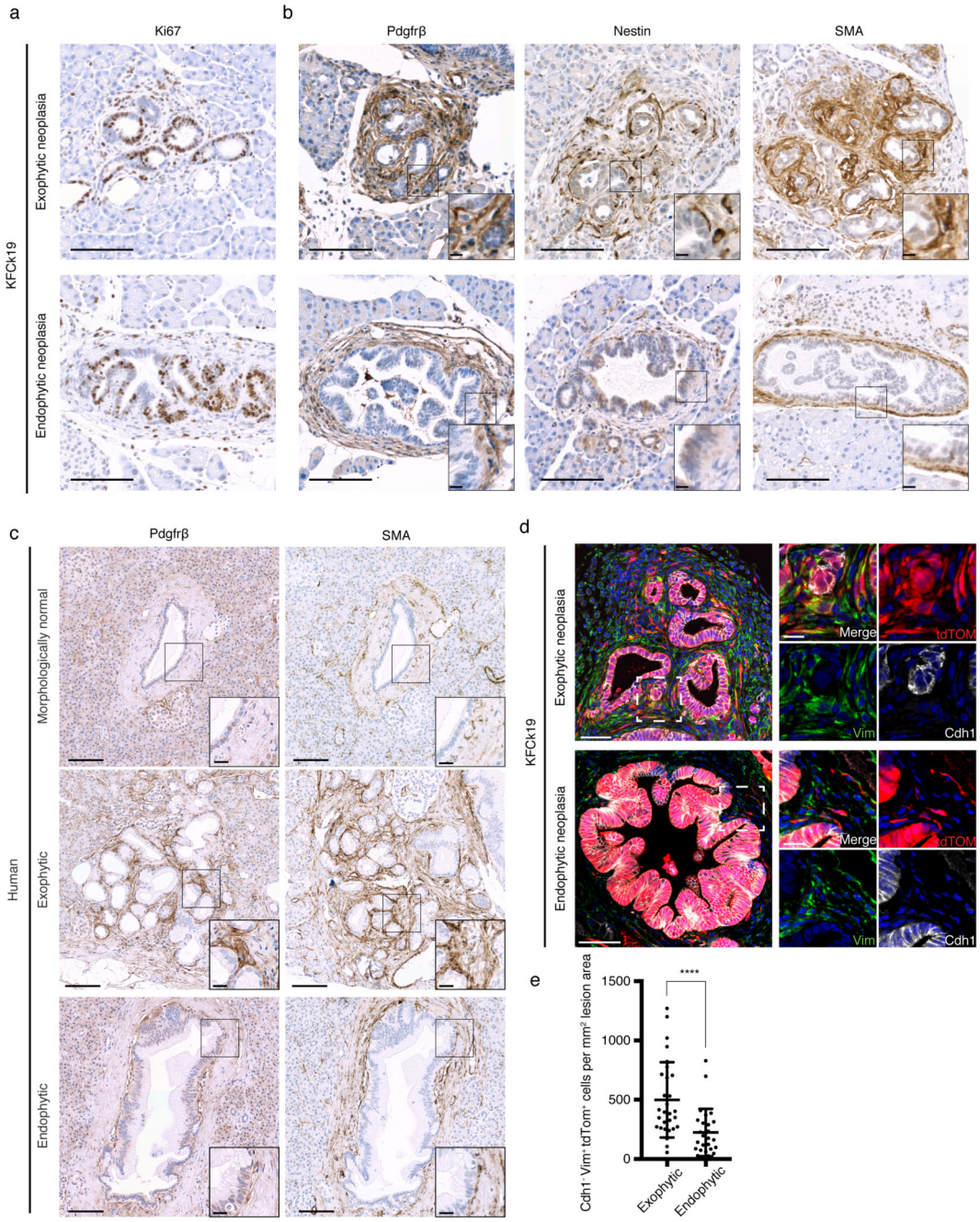

Extended Data Figure 5. Characterisation of exophytic and endophytic neoplasia biology.

(a) Proliferation of exophytic and endophytic lesions of KFCk19 mice as indicated by Ki67. Scale bar 100 μm. Representative of 3 mice. **(b)** Stromal composition of KFCk19 exophytic and endophytic lesions 3 weeks after recombination and recruitment of cancer-associated fibroblasts (CAFs) as demonstrated by staining for Pdgfrβ, nestin and smooth muscle actin (SMA). For staining comparison between endophytic and exophytic lesions, lesions in the same tissue section are shown. Scale bars 100 μm. Insets show magnified views of the area indicated. Scale bars 10 μm. Representative of 4 mice. **(c)** Staining for human CAF markers

Pdgfrβ and SMA in background pancreatic tissue of a PDAC patient. Shown are an example of a non-dysplastic duct, an exophytic lesion, and an endophytic lesion from the same tissue section. Scale bars 100 μm. Insets show magnified views of the area indicated. Scale bars 20 μm. 1 patient. **(d)** Tumour cell epithelial-to-mesenchymal transition (EMT) in advanced KFCk19 exophytic and endophytic lesions 8 weeks after recombination. Scale bars 50 μm. Indicated areas are magnified on the right. Scale bars 15 μm. Cdh1 staining marks epithelial cells, vimentin (Vim) staining indicates mesenchymal character and tdTomato identifies tumour-traced cells. Representative of 3 mice. **(e)** Quantification of EMT in (d) as the number of tdTomato-traced, $Cdh1^-$, Vim^+ cells per lesion area. Exophytic, n=29 lesions; endophytic n=26 lesions. Data are mean ± s.d., ****P <0.0001 (two-sided Mann-Whitney test).

Europe PMC Funders Author Manuscripts

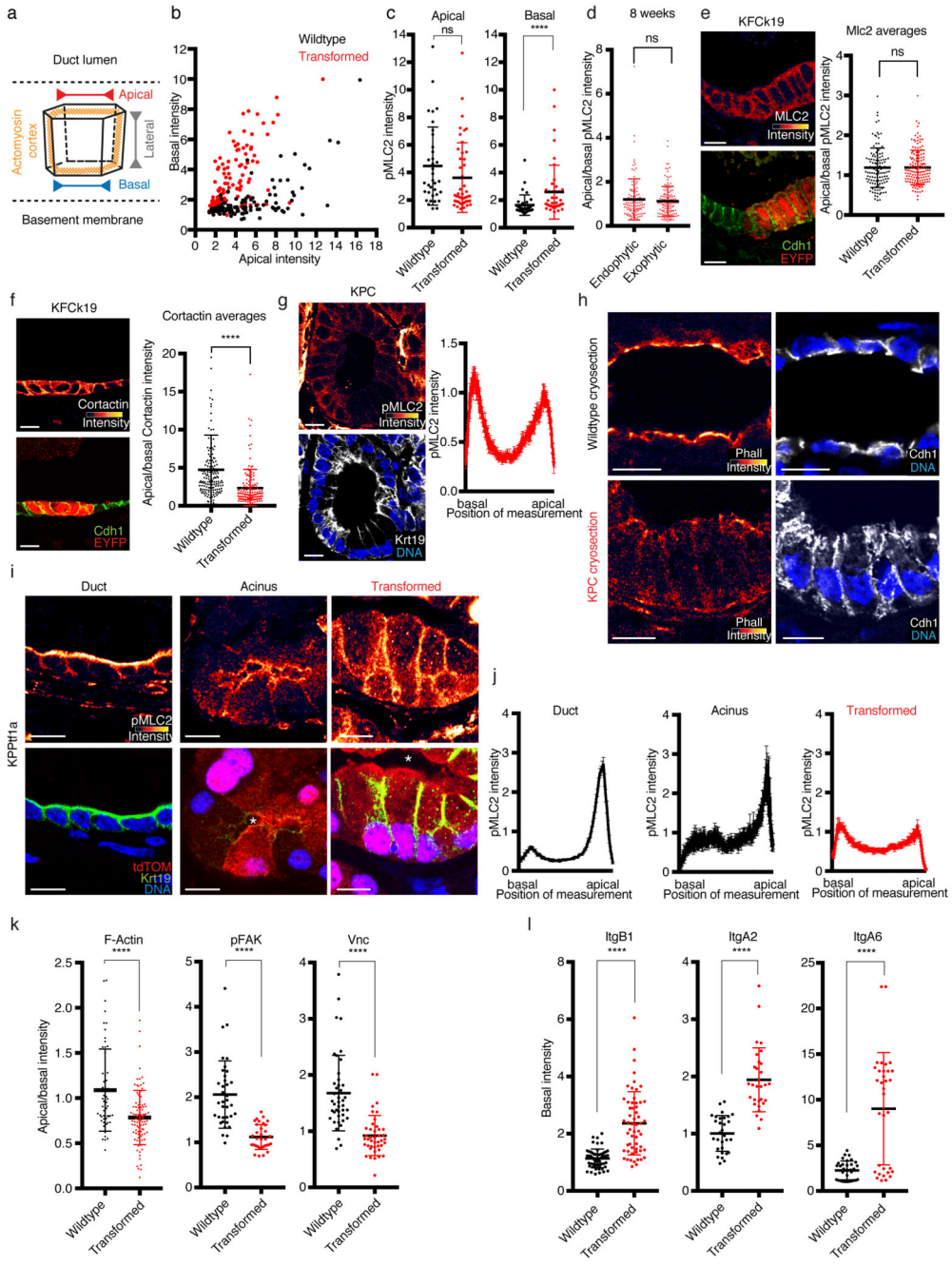

Extended Data Figure 6. Cortical alterations in transformed cells.

(a) Schematic showing cell orientation and cell cortex organisation. **(b)** Scatterplot of apical-basal pMLC2 intensities per cell from endophytic and exophytic lesions in KFCk19 mice. Wildtype, 106 cells; transformed, 124 cells. **(c)** Basal and apical pMLC2 intensities were extracted from the maxima of the intensity profiles of each cell from exophytic lesions (Fig. 2i) (wildtype 35 cells, transformed 45 cells). Data are mean ± s.d., ns – not significant P=0.057, ****P <0.0001 (two-sided Mann-Whitney test). **(d)** Ratio of apical/basal pMLC2 intensity in late stage exophytic and endophytic lesions 8 weeks after recombination

Europe PMC Funders Author Manuscripts

(KFCk19). Endophytic, 110 cells; exophytic 138 cells. Data are mean ± s.d., ns – not significant (two-sided Mann-Whitney test). **(e)** MLC2 distribution in transformed and wildtype cells of KFCk19 mice. Left, immunofluorescence staining for MLC2, Cdh1 and EYFP. Scale bar 10 μm. Right, Ratio of apical/basal MLC2 intensity. Wildtype, 119 cells; transformed, 139 cells. Data are mean ± s.d., ns – not significant P=0.7722 (two-sided Mann-Whitney test). **(f)** Cortactin distribution in transformed and wildtype cells of KFCk19 mice. Left, immunofluorescence staining for cortactin, Cdh1 and EYFP. Scale bar 10 μm. Right, Ratio of apical/basal cortactin intensity. Wildtype, 152 cells; transformed, 137 cells. Data are mean ± s.d., ****P <0.0001 (two-sided Mann-Whitney test). **(g)** pMLC2 distribution in the KPC model. Left, immunofluorescence staining for pMLC2 and Krt19. Scale bar 10 μm. Right, Basal-apical pMLC2 intensity profile, measured as shown in Fig. 2h. Single cell profiles were normalised to cellular average and aligned in length. Data are mean ± s.e.m. (157 cells). **(h)** F-actin distribution in the KPC model. Immunofluorescence staining for F-actin (phalloidin) and Cdh1 on cryosectioned pancreata from KPC mice or wildtype littermates. Scale bar 10 μm. Quantifications are shown in Fig. 2k. Wildtype, 4 mice; Transformed, 3 mice **(i-j)** pMLC2 distribution in the KPPtf1a model of acinar cell transformation. **(i)** Immunofluorescence staining for pMLC2, Krt19 and td-Tomato. Scale bars 10 μm. Left, normal duct; middle, normal Krt19-negative acinus; right, transformed Krt19-positive tdTomato traced cells. Asterisk indicates lumen. Representative of 3 mice. **(j)** Basal-apical pMLC2 intensity profiles, measured as shown in Fig. 2h. Single cell profiles were normalised to cellular average and aligned in length. Data are mean ± s.e.m. (normal duct, 142 cells; normal acinus, 76 cells; transformed, 127 cells). **(k)** Ratio of apical/basal F-actin, pFak and Vinculin (Vnc) intensities in wildtype and transformed cells of KFCk19 mice. (F-actin, 57 wildtype cells, 93 transformed cells; Vnc, 42 wildtype cells, 42 transformed cells; pFAK, 36 wildtype cells, 36 transformed cells). Data are mean ± s.d., ****P <0.0001 (two-sided Mann-Whitney test). **(l)** Expression of integrins in transformed cells relative to wildtype duct cell neighbours in KFCk19 mice. (ItgA2, 57 wildtype cells, 57 transformed cells; ItgA6, 33 wildtype cells, 33 transformed cells; ItgB1, 30 wildtype cells, 30 transformed cells). Data are mean ± s.d., ****P <0.0001 (two-sided Mann-Whitney test).

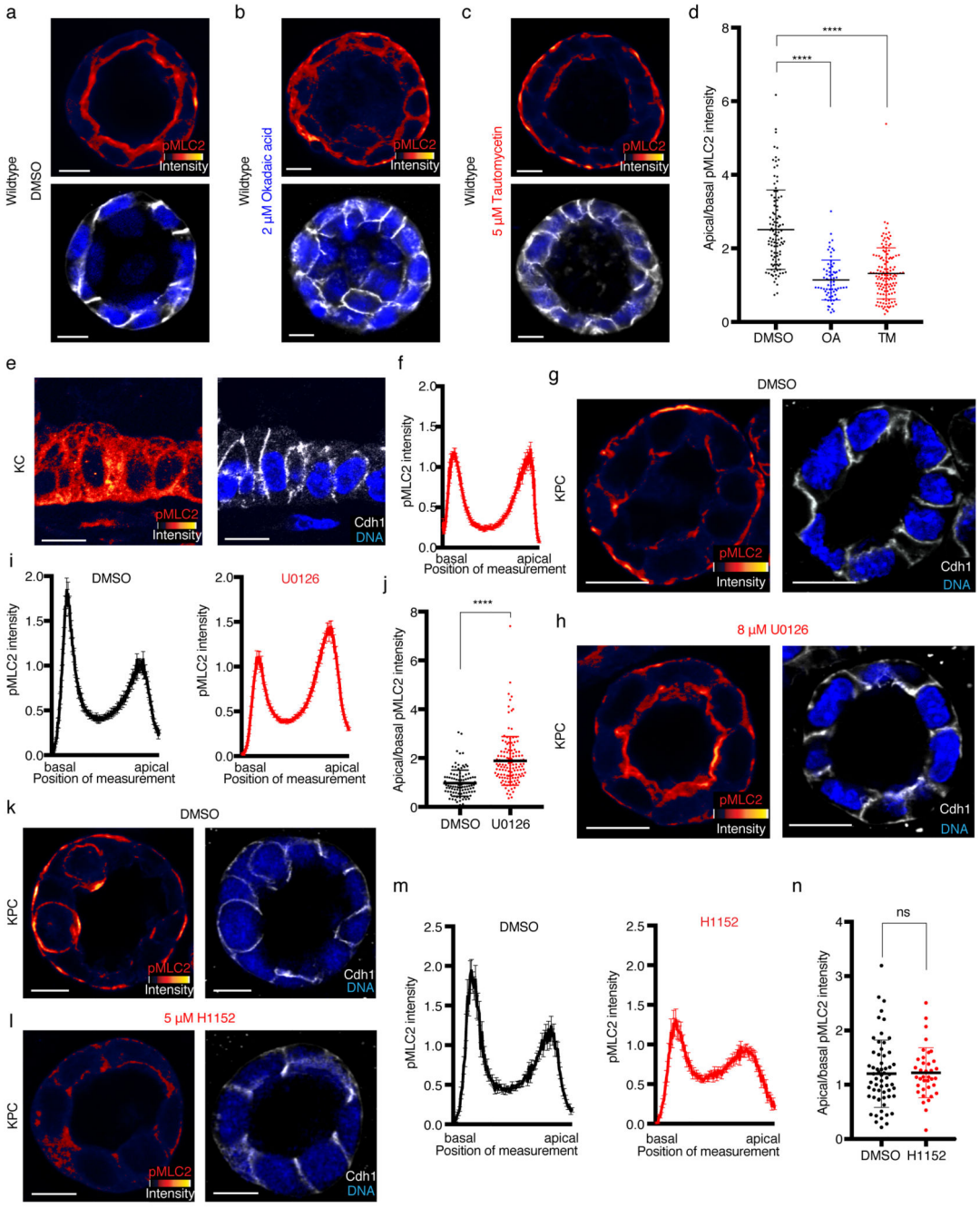

Extended Data Figure 7. Role of oncogenic Kras signalling in the pMLC2 distribution of transformed epithelial cells.

(a-d) pMLC2 distribution in wildtype organoids after phosphatase inhibition. **(a-c)** Immunostaining for pMLC2 and Cdh1. Scale bars 10 µm. Representatives of 2 experiments with 3 wildtype organoid lines. **(a)** DMSO control. **(b)** 2 µM okadaic acid treatment. **(c)** 5 µM tautomycetin treatment. **(d)** Ratio of apical/basal pMLC2 intensity of wildtype organoids after treatment with DMSO, okadaic acid (OA) or tautomycetin (TM). DMSO, 104 cells; okadaic acid, 70 cells; tautomycetin, 131 cells. Data are mean ± s.d., ****P <0.0001 (two-

Europe PMC Funders Author Manuscripts

sided Mann-Whitney test). **(e)** pMLC2 distribution in *KrasG12D; Pdx1-Cre* mice (KC). Immunostaining for pMLC2 and Cdh1. Scale bar 10 μm. Representative of 2 mice. **(f)** Basal-apical pMLC2 intensity profile of KC cells (e), measured as shown in Fig. 2h. Single cell profiles were normalised to cellular average and aligned in length. Data are mean ± s.e.m. (219 cells). **(g-j)** pMLC2 distribution in KPC organoids after MEK inhibition. **(g-h)** Immunostaining for pMLC2 and Cdh1. Scale bars 20 μm. Representatives of 3 experiments with 3 KPC organoid lines. **(g)** DMSO control. **(h)** 8 μM U0126 treatment. **(i)** Basal-apical pMLC2 intensity profiles of DMSO or U0126-treated organoids, measured as shown in Fig. 2h. Single cell profiles were normalised to cellular average and aligned in length. Data are mean ± s.e.m. (105 cells DMSO, 133 cells U0126). **(j)** Ratio of apical/basal pMLC2 intensity of KPC organoids after DMSO or U0126 treatment. DMSO, 105 cells; U0126, 133 cells. Data are mean ± s.d., ****P <0.0001 (two-sided Mann-Whitney test). **(k-l)** Immunostaining for pMLC2 and Cdh1. Scale bars 20 μm. **(k)** DMSO control. **(l)** 5 μM ROCK inhibitor (H1152) treatment. Representatives of 2 experiments with 3 KPC organoid lines. **(m)** Basal-apical pMLC2 intensity profiles of DMSO or H1152-treated organoids, measured as shown in Fig. 2h. Single cell profiles were normalised to cellular average and aligned in length. Data are mean ± s.e.m. (59 cells DMSO, 38 cells H1152). **(n)** Ratio of apical/basal pMLC2 intensity of KPC organoids after DMSO or H1152 treatment. DMSO, 60 cells; H1152, 37 cells. Data are mean ± s.d., ns - not significant P=0.5517 (two-sided Mann-Whitney test).

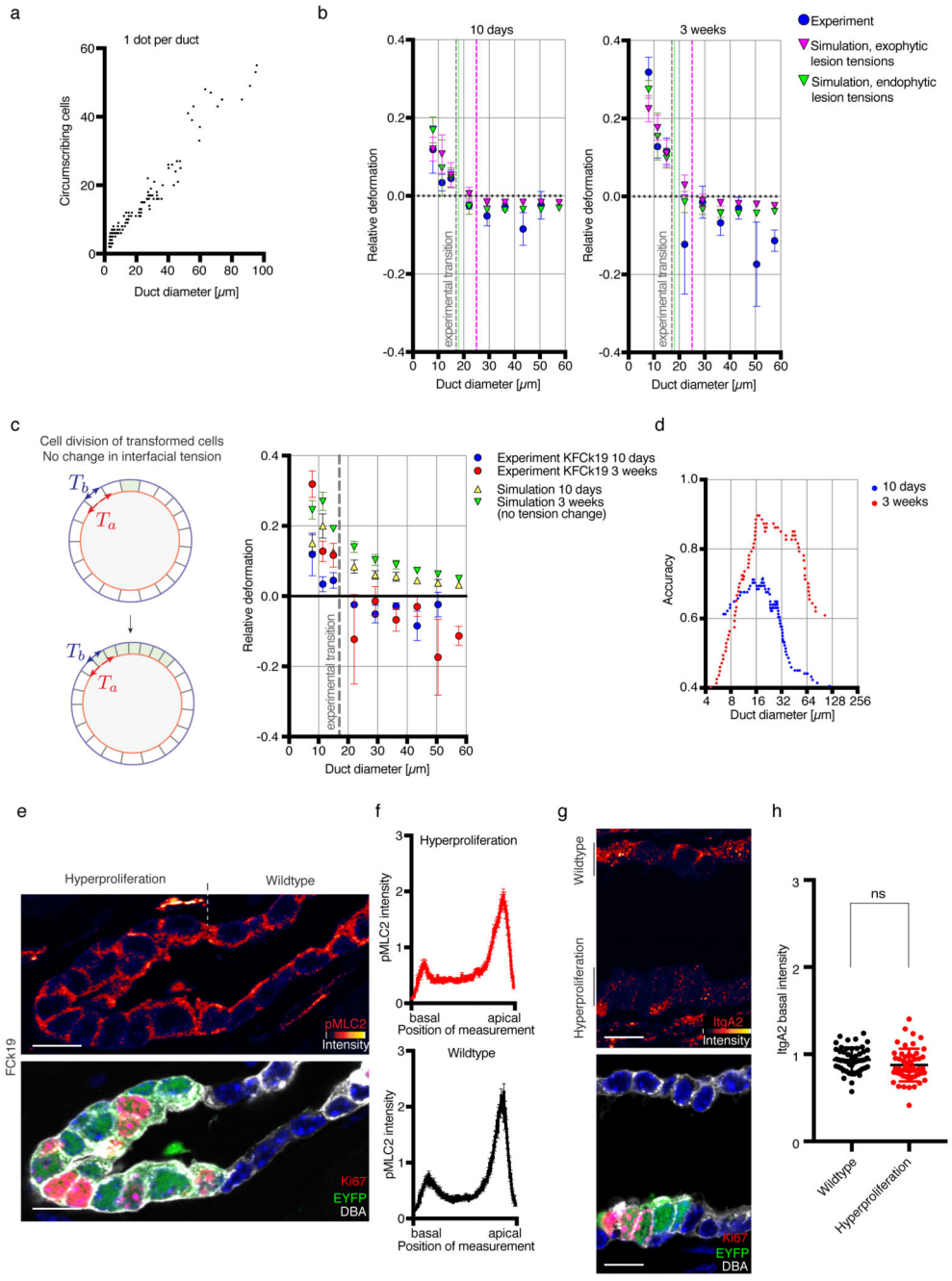

Extended Data Figure 8. Formulation of ductal transformation in the 3D vertex model and the effect of tension change.

(a) Number of circumscribing cells per duct diameter (113 ducts, 8 mice). **(b)** Relative deformation as a function of diameter (mean ± s.e.m. from N=10 simulations), for simulations with tension changes derived from exophytic (pink) and endophytic lesions (green). Both inputs produce deformations in good agreement with experimental observations (blue). **(c)** Simulation of hyperproliferation without mechanical changes is not sufficient to explain the transition between exophytic and endophytic lesions (dots indicate

Europe PMC Funders Author Manuscripts

mean ± s.e.m. from N=10 simulations). Experimental data from Fig. 3d are shown for comparison. Simulations were carried out as in Fig. 3d, except that mechanical parameters in transformed cells were not modified. **(d)** Classification accuracy, defined as the fraction of exophytic and endophytic lesions that can be predicted based on duct diameter, as a function of duct diameter. The accuracy is defined for each diameter d as (TP+TN)/(TP+FP+TN +FN), where TP (true positive) and FP (false positive) denote the number of exophytic and endophytic deformations occurring below diameter d, TN (true negative) and FN (false negative) denote the number of endophytic and exophytic deformations occurring above diameter d. The diameter of maximal accuracy at 3 weeks is used to find the location of the transition. **(e)** Immunofluorescence staining for pMLC2, Ki67, DBA and EYFP showing pMLC2 distribution in hyperproliferating cells and wildtype duct cell neighbours of *Fbw7 F/F; Ck19-CreERt* (FCk19) mice. Scale bars 10 μm. Representative of 6 mice. **(f)** Basal-apical pMLC2 pixel intensity profiles of normal and hyperproliferating cells. Single cell profiles were normalised to cellular average and aligned in length. Data are mean ± s.e.m. 28 ducts (6 mice), n=64 *Fbw7 F/F* cells, n=93 wildtype cells. **(g)** Immunofluorescence staining for ItgA2, Ki67, DBA and EYFP showing lack of basal integrin overexpression in hyperproliferating cells and wildtype duct cell neighbours of FCk19 mice. Scale bars 10 μm. Representative of 3 mice. **(h)** Quantification of basal ItgA2 localisation in hyperproliferative cells relative to wildtype duct cell neighbours. (n=52 wildtype cells, 51 *Fbw7 F/F* cells). Data are mean ± s.d., ns – not significant).

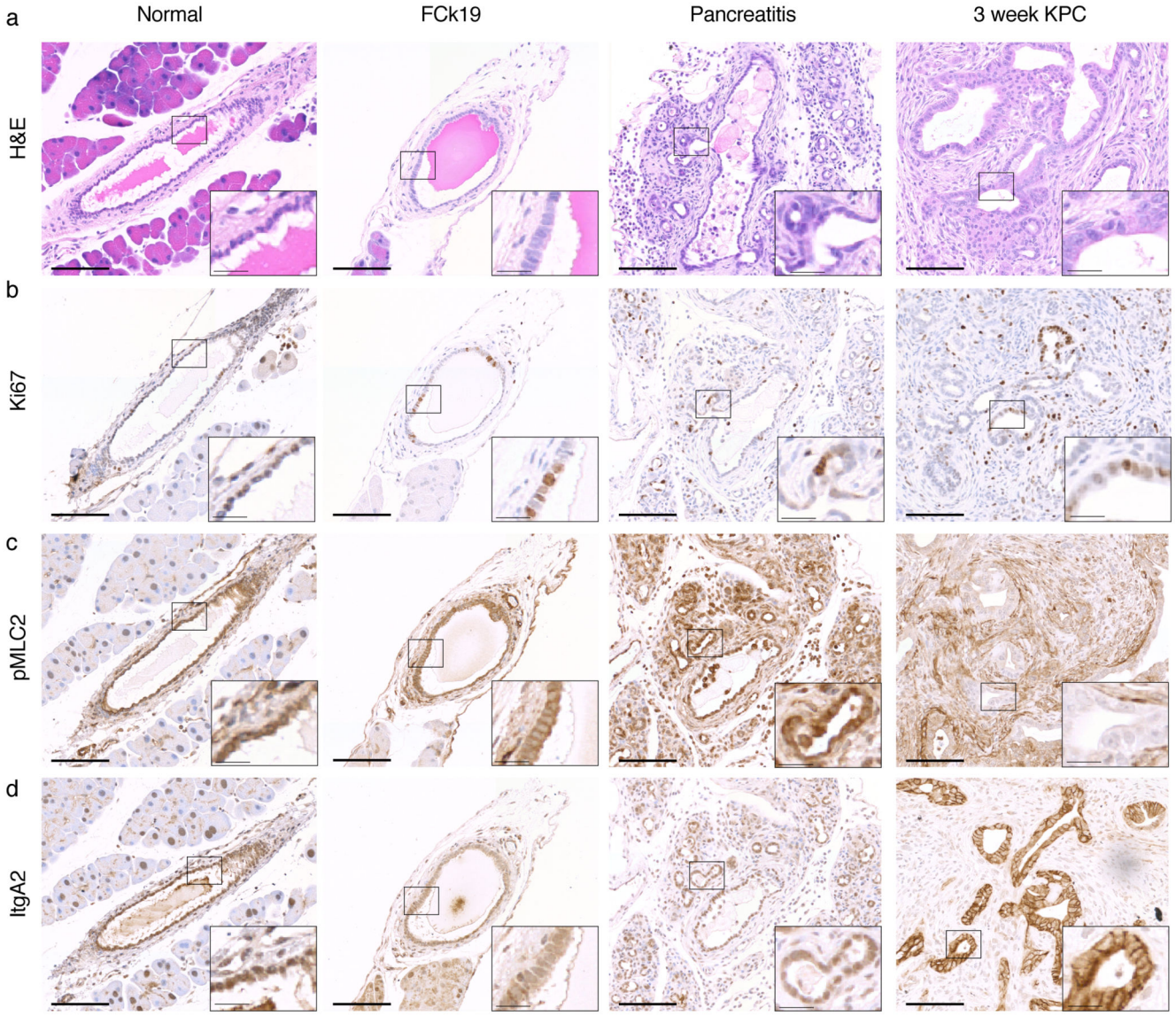

Extended Data Figure 9. Histological differentiation of benign and malignant ductal reactions.
(a) Left to right, H&E stain of normal pancreas, FCk19 pancreas (hyperproliferative ducts), acute caerulein-induced pancreatitis and 3-week-old KPC mice. **(b)** Ki67 staining demonstrating proliferation in FCk19 ducts, ductal structures of acute pancreatitis and early transformation (KPC). **(c)** Staining for pMLC2 showing apical-basal redistribution of pMLC2 in transformed ductal lesions (KPC) but not in normal duct cells (left), FCk19 ducts and reactive ducts. **(d)** ItgA2 is absent from the cellular membrane in normal duct cells (left) and FCk19 ducts and reactive ducts, but highly abundant in transformed ductal lesions (KPC). All scale bars 100 μm, all inset scale bars 20 μm. All stainings representative of 6 mice (normal pancreas), 4 mice (FCk19), 4 mice (acute pancreatitis), 3 mice (KPC).

Europe PMC Funders Author Manuscripts

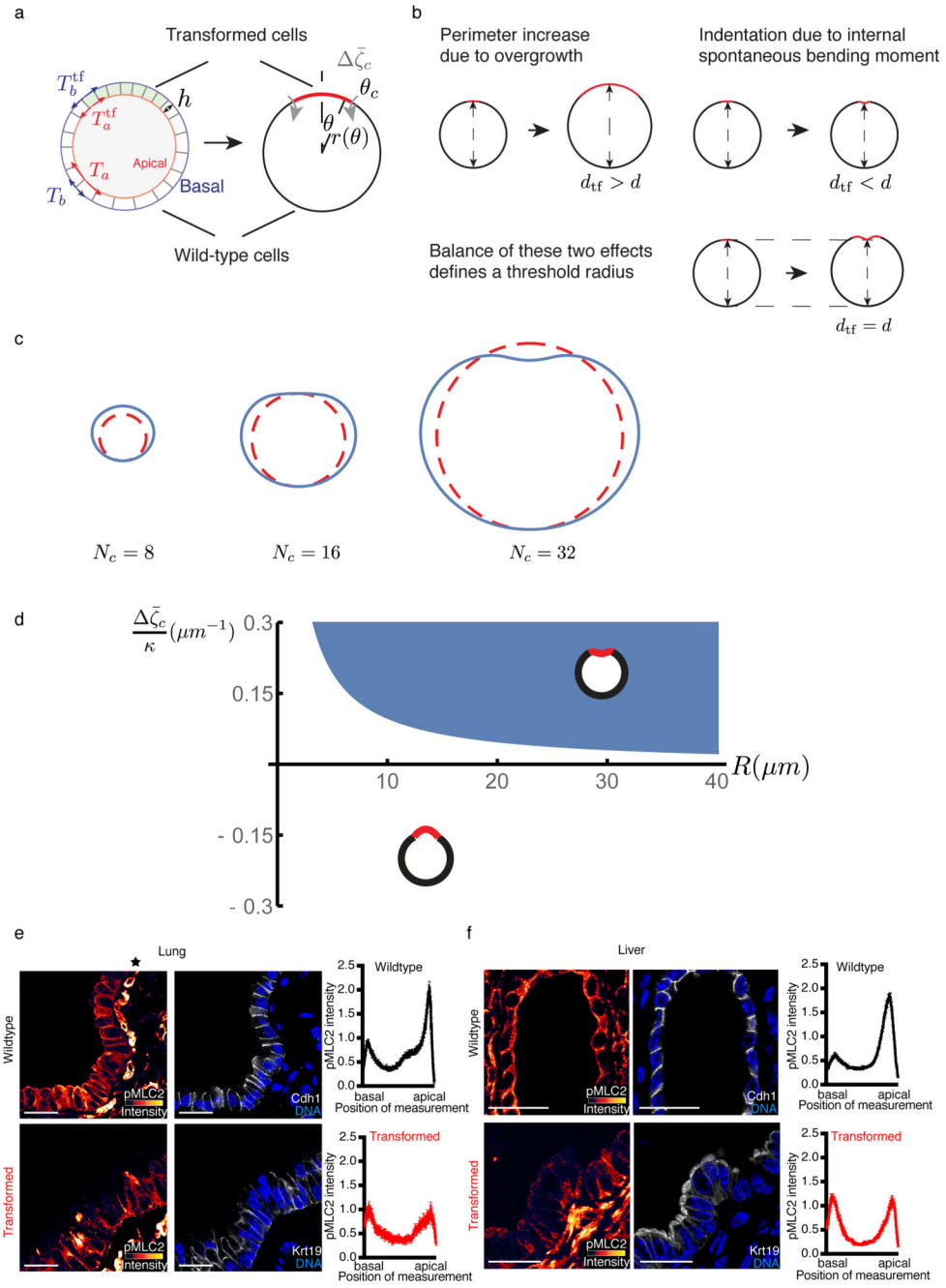

Extended Data Figure 10. Continuum theory of early lesion morphogenesis and pMLC2 distribution in lung airways and hepatic ducts.

(a) We consider a continuum theory of tissue mechanics where the tissue is represented by a thin layer. The tissue has initially the shape of a cylinder, and we consider for simplicity deformations that are invariant along the longitudinal axis in cylindrical coordinates. The tissue has a bending elasticity and an area stretch elasticity resisting its deformation. In addition, the transformed region is subjected to a spontaneous bending moment difference $\Delta \bar{\zeta}_c$ compared to the wild-type tissue. The spontaneous bending moment arises from the

difference between the tissue basal and apical surface tension T_b and T_a In the transformed tissue, the apical and basal surface tension T_a^{tf} and T_b^{tf} differ from their values in the wild-type tissue, T_a and $_b$ **(b)** Two effects drive tissue deformation: tissue growth due to transformed cell division and growth leads to an increase in the radius of the cylindrical tissue, while the spontaneous bending moment difference drives an inward invagination. The balance of these two effects on the transformed tissue indentation defines a threshold radius where the indentation of the transformed tissue along the axis of symmetry vanishes. **(c)** Calculated deformed tissue cross-sections after the introduction of a region of transformed cells, in the limit of small deformations. Blue line, deformed shape; red dotted line, original shape; the transformed cells are in the upper region. N_c is the number of cells in a tissue cross-section prior to cell transformation. Other parameters: $\frac{\Delta \bar{\xi}_c l_0}{\kappa} = 0.39$, $N_t = 3$ transformed cells in a cross-section. **(d)** Phase diagram of direction of tumour deformation, in the limit of small deformations and small transformed region. R is the cylinder radius, $\Delta \bar{\xi}_c$ the spontaneous bending moment difference in the transformed tissue, and κ the tissue bending modulus. Schematic examples of tissue cross-sections undergoing inward (blue area) and outward (white area) deformations are shown. **(e)** pMLC2 distribution in lung airways. Left, immunostaining for pMLC2 and Cdh1 in KFCk19 transformed and wildtype epithelium. Star marks pMLC2 high myofibroblasts located below the epithelium. Scale bars 20 μm. Right, Basal-apical pMLC2 intensity profiles, measured as shown in Fig. 2h. Single cell profiles were normalised to cellular average and aligned in length. Data are mean ± s.e.m. (wildtype, 167 cells; transformed, 66 cells). **(f)** pMLC2 distribution in hepatic ducts. Left, immunostaining for pMLC2 and Cdh1 in KFCk19 transformed and wildtype epithelium. Scale bars 20 μm. Right, Basal-apical pMLC2 intensity profiles, measured as shown in Fig. 2h. Single cell profiles were normalised to cellular average and aligned in length. Data are mean ± s.e.m. (wildtype, 134 cells; transformed, 284 cells).

Supplementary Material

Refer to Web version on PubMed Central for supplementary material.

Acknowledgments

We thank C. Cremona, V. Gebala, M. Popovic, N. Tapon and B. Thompson for comments on the manuscript and the Francis Crick Institute Biological Research, Experimental Histopathology and Light Microscopy facilities for technical support. This work was supported by the Francis Crick Institute, which receives its core funding from Cancer Research UK (FC001039, FC001317), the UK Medical Research Council (FC001039, FC001317) and the Wellcome Trust (FC001039, FC001317). This work was also supported by an ERC grant to A.B. (281661).

References

1. Bailey JM, et al. p53 mutations cooperate with oncogenic Kras to promote adenocarcinoma from pancreatic ductal cells. Oncogene. 2016; 35:4282–4288. DOI: 10.1038/onc.2015.441 [PubMed: 26592447]
2. Ferreira RMM, et al. Duct- and Acinar-Derived Pancreatic Ductal Adenocarcinomas Show Distinct Tumor Progression and Marker Expression. Cell Rep. 2017; 21:966–978. DOI: 10.1016/j.celrep.2017.09.093 [PubMed: 29069604]

3. Ferone G, et al. SOX2 Is the Determining Oncogenic Switch in Promoting Lung Squamous Cell Carcinoma from Different Cells of Origin. Cancer Cell. 2016; 30:519–532. DOI: 10.1016/j.ccell.2016.09.001 [PubMed: 27728803]
4. Guest RV, et al. Cell lineage tracing reveals a biliary origin of intrahepatic cholangiocarcinoma. Cancer Res. 2014; 74:1005–1010. DOI: 10.1158/0008-5472.CAN-13-1911 [PubMed: 24310400]
5. Paszek MJ, et al. Tensional homeostasis and the malignant phenotype. Cancer Cell. 2005; 8:241–254. DOI: 10.1016/j.ccr.2005.08.010 [PubMed: 16169468]
6. Zhang Q, et al. Fbxw7 Deletion Accelerates Kras(G12D)-Driven Pancreatic Tumorigenesis via Yap Accumulation. Neoplasia. 2016; 18:666–673. DOI: 10.1016/j.neo.2016.08.009 [PubMed: 27764699]
7. Rhim AD, et al. EMT and dissemination precede pancreatic tumor formation. Cell. 2012; 148:349–361. DOI: 10.1016/j.cell.2011.11.025 [PubMed: 22265420]
8. Hanahan D, Coussens LM. Accessories to the crime: functions of cells recruited to the tumor microenvironment. Cancer Cell. 2012; 21:309–322. DOI: 10.1016/j.ccr.2012.02.022 [PubMed: 22439926]
9. Ohlund D, et al. Distinct populations of inflammatory fibroblasts and myofibroblasts in pancreatic cancer. J Exp Med. 2017; 214:579–596. DOI: 10.1084/jem.20162024 [PubMed: 28232471]
10. Heer NC, Martin AC. Tension, contraction and tissue morphogenesis. Development. 2017; 144:4249–4260. DOI: 10.1242/dev.151282 [PubMed: 29183938]
11. Goeckeler ZM, Wysolmerski RB. Myosin light chain kinase-regulated endothelial cell contraction: the relationship between isometric tension, actin polymerization, and myosin phosphorylation. J Cell Biol. 1995; 130:613–627. [PubMed: 7622562]
12. Elliott H, et al. Myosin II controls cellular branching morphogenesis and migration in three dimensions by minimizing cell-surface curvature. Nat Cell Biol. 2015; 17:137–147. DOI: 10.1038/ncb3092 [PubMed: 25621949]
13. Lomakin AJ, et al. Competition for actin between two distinct F-actin networks defines a bistable switch for cell polarization. Nat Cell Biol. 2015; 17:1435–1445. DOI: 10.1038/ncb3246 [PubMed: 26414403]
14. Heid I, et al. Early requirement of Rac1 in a mouse model of pancreatic cancer. Gastroenterology. 2011; 141:719–730, 730 e711-717. DOI: 10.1053/j.gastro.2011.04.043 [PubMed: 21684285]
15. Baer R, et al. Pancreatic cell plasticity and cancer initiation induced by oncogenic Kras is completely dependent on wild-type PI 3-kinase p110alpha. Genes & development. 2014; 28:2621–2635. DOI: 10.1101/gad.249409.114 [PubMed: 25452273]
16. Pickup MW, Mouw JK, Weaver VM. The extracellular matrix modulates the hallmarks of cancer. EMBO Rep. 2014; 15:1243–1253. DOI: 10.15252/embr.201439246 [PubMed: 25381661]
17. Schafer C, et al. Differential Kras(V12) protein levels control a switch regulating lung cancer cell morphology and motility. Converg Sci Phys Oncol. 2016; 2doi: 10.1088/2057-1739/2/3/035004
18. Magudia K, Lahoz A, Hall A. K-Ras and B-Raf oncogenes inhibit colon epithelial polarity establishment through up-regulation of c-myc. J Cell Biol. 2012; 198:185–194. DOI: 10.1083/jcb.201202108 [PubMed: 22826122]
19. Mendoza MC, Vilela M, Juarez JE, Blenis J, Danuser G. ERK reinforces actin polymerization to power persistent edge protrusion during motility. Sci Signal. 2015; 8:ra47.doi: 10.1126/scisignal.aaa8859 [PubMed: 25990957]
20. Nguyen DHD, et al. Myosin Light Chain Kinase Functions Downstream of Ras/ERK to Promote Migration of Urokinase-Type Plasminogen Activator-Stimulated Cells in an Integrin-Selective Manner. The Journal of Cell Biology. 1999; 146:149–164. DOI: 10.1083/jcb.146.1.149 [PubMed: 10402467]
21. Shen Q, Rigor RR, Pivetti CD, Wu MH, Yuan SY. Myosin light chain kinase in microvascular endothelial barrier function. Cardiovasc Res. 2010; 87:272–280. DOI: 10.1093/cvr/cvq144 [PubMed: 20479130]
22. Bielmeier C, et al. Interface Contractility between Differently Fated Cells Drives Cell Elimination and Cyst Formation. Curr Biol. 2016; 26:563–574. DOI: 10.1016/j.cub.2015.12.063 [PubMed: 26853359]

23. Alt S, Ganguly P, Salbreux G. Vertex models: from cell mechanics to tissue morphogenesis. Philos Trans R Soc Lond B Biol Sci. 2017; 372doi: 10.1098/rstb.2015.0520
24. Clark AG, Wartlick O, Salbreux G, Paluch EK. Stresses at the cell surface during animal cell morphogenesis. Curr Biol. 2014; 24:R484–494. DOI: 10.1016/j.cub.2014.03.059 [PubMed: 24845681]
25. Sancho R, Gruber R, Gu G, Behrens A. Loss of Fbw7 Reprograms Adult Pancreatic Ductal Cells into alpha, delta, and beta Cells. Cell stem cell. 2014; 15:139–153. DOI: 10.1016/j.stem.2014.06.019 [PubMed: 25105579]
26. Reichert M, Rustgi AK. Pancreatic ductal cells in development, regeneration, and neoplasia. The Journal of clinical investigation. 2011; 121:4572–4578. DOI: 10.1172/JCI57131 [PubMed: 22133881]
27. Marchetti MC, et al. Hydrodynamics of soft active matter. Reviews of Modern Physics. 2013; 85:1143–1189. DOI: 10.1103/RevModPhys.85.1143
28. Prost J, Jülicher F, Joanny JF. Active gel physics. Nature Physics. 2015; 11:111–117. DOI: 10.1038/nphys3224
29. Salbreux G, Jülicher F. Mechanics of active surfaces. Physical Review E. 2017; 96doi: 10.1103/PhysRevE.96.032404
30. Means AL, Xu Y, Ray KC, Gu G. A CK19(CreERT) knockin mouse line allows for conditional DNA recombination in epithelial cells in multiple endodermal organs. Genesis (New York, NY : 2000). 2008; 46:318–323. DOI: 10.1002/dvg.20397
31. Desai BM, et al. Preexisting pancreatic acinar cells contribute to acinar cell, but not islet [beta] cell, regeneration. The Journal of clinical investigation. 2007; 117
32. Solar M, et al. Pancreatic exocrine duct cells give rise to insulin-producing beta cells during embryogenesis but not after birth. Developmental cell. 2009; 17:849–860. DOI: 10.1016/j.devcel.2009.11.003 [PubMed: 20059954]
33. Hingorani SR, et al. Preinvasive and invasive ductal pancreatic cancer and its early detection in the mouse. Cancer cell. 2003; 4:437–450. [PubMed: 14706336]
34. Pan FC, et al. Spatiotemporal patterns of multipotentiality in Ptf1a-expressing cells during pancreas organogenesis and injury-induced facultative restoration. Development. 2013; 140:751–764. DOI: 10.1242/dev.090159 [PubMed: 23325761]
35. Jackson EL, et al. Analysis of lung tumor initiation and progression using conditional expression of oncogenic K-ras. Genes & development. 2001; 15:3243–3248. [PubMed: 11751630]
36. Hoeck JD, et al. Fbw7 controls neural stem cell differentiation and progenitor apoptosis via Notch and c-Jun. Nat Neurosci. 2010; 13:1365–1372. DOI: 10.1038/nn.2644 [PubMed: 20935640]
37. Hara M, et al. Transgenic mice with green fluorescent protein-labeled pancreatic beta -cells. Am J Physiol Endocrinol Metab. 2003; 284:E177–183. DOI: 10.1152/ajpendo.00321.2002 [PubMed: 12388130]
38. Marino S, Vooijs M, van Der Gulden H, Jonkers J, Berns A. Induction of medulloblastomas in p53-null mutant mice by somatic inactivation of Rb in the external granular layer cells of the cerebellum. Genes & development. 2000; 14:994–1004. [PubMed: 10783170]
39. Snippert HJ, et al. Intestinal crypt homeostasis results from neutral competition between symmetrically dividing Lgr5 stem cells. Cell. 2010; 143:134–144. DOI: 10.1016/j.cell.2010.09.016 [PubMed: 20887898]
40. Madisen L, et al. A robust and high-throughput Cre reporting and characterization system for the whole mouse brain. Nat Neurosci. 2010; 13:133–140. DOI: 10.1038/nn.2467 [PubMed: 20023653]
41. Srinivas S, et al. Cre reporter strains produced by targeted insertion of EYFP and ECFP into the ROSA26 locus. BMC Dev Biol. 2001; 1:4. [PubMed: 11299042]
42. Huch M, et al. Unlimited in vitro expansion of adult bi-potent pancreas progenitors through the Lgr5/R-spondin axis. The EMBO journal. 2013; 32:2708–2721. DOI: 10.1038/emboj.2013.204 [PubMed: 24045232]
43. Boj SF, et al. Organoid models of human and mouse ductal pancreatic cancer. Cell. 2015; 160:324–338. DOI: 10.1016/j.cell.2014.12.021 [PubMed: 25557080]

Europe PMC Funders Author Manuscripts

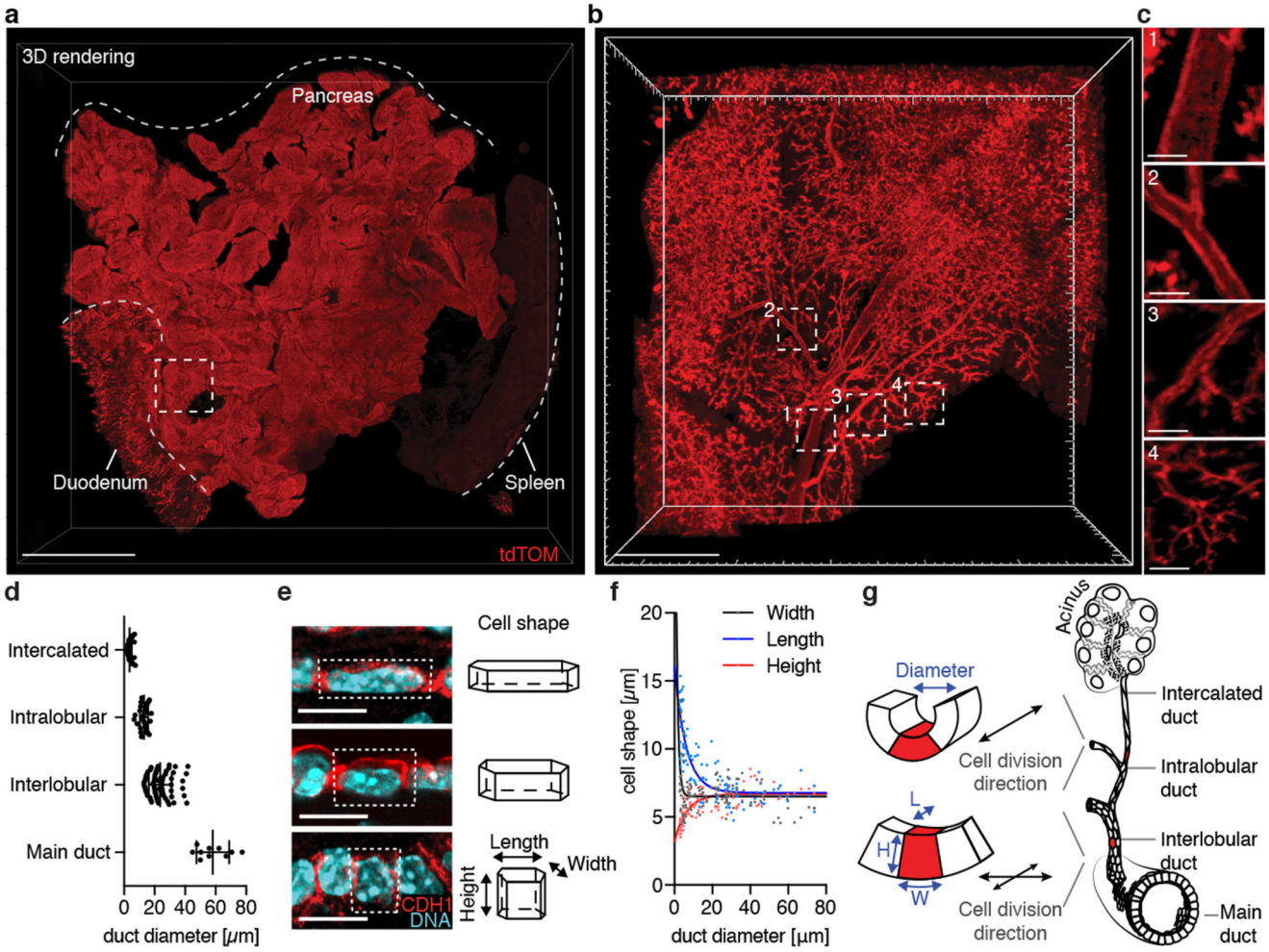

Fig. 1. FLASH imaging of the intact pancreas and visualisation of the ductal tree.

a-c, 3D views of an intact pancreas from tamoxifen-treated *R26-CAG-tdTomato; Hnf1βCreERT2* mouse. n=3 mice. **a**, Whole pancreas attached to duodenum and spleen. **b**, Enlargement of area in (**a**). **c**, Ductal segments: **1**, main duct; **2**, interlobular duct; **3**, intralobular duct; **4**, intercalated ducts. **d**, Segmental heterogeneity of duct diameter. Mean ± s.d., n=11 main ducts, n=67 interlobular ducts, n=34 intralobular ducts, n=72 intercalated ducts from 3 mice. **e**, Pancreas tissue section stained for Cdh1 and DNA to highlight duct cell shapes. n=4 mice. **f**, Segmental heterogeneity of duct cell width (black), height (red) and length (blue); averages of five cells per duct, n=115 ducts from 6 mice. Fitted lines obtained using nonlinear regression. **g**, Segmental heterogeneity of the ductal tree. L – cell length, W – cell width, H – cell height. Scale bars, 5 mm (**a**), 500 μm (**b**), 100 μm (**c**), 10 μm (**e**).

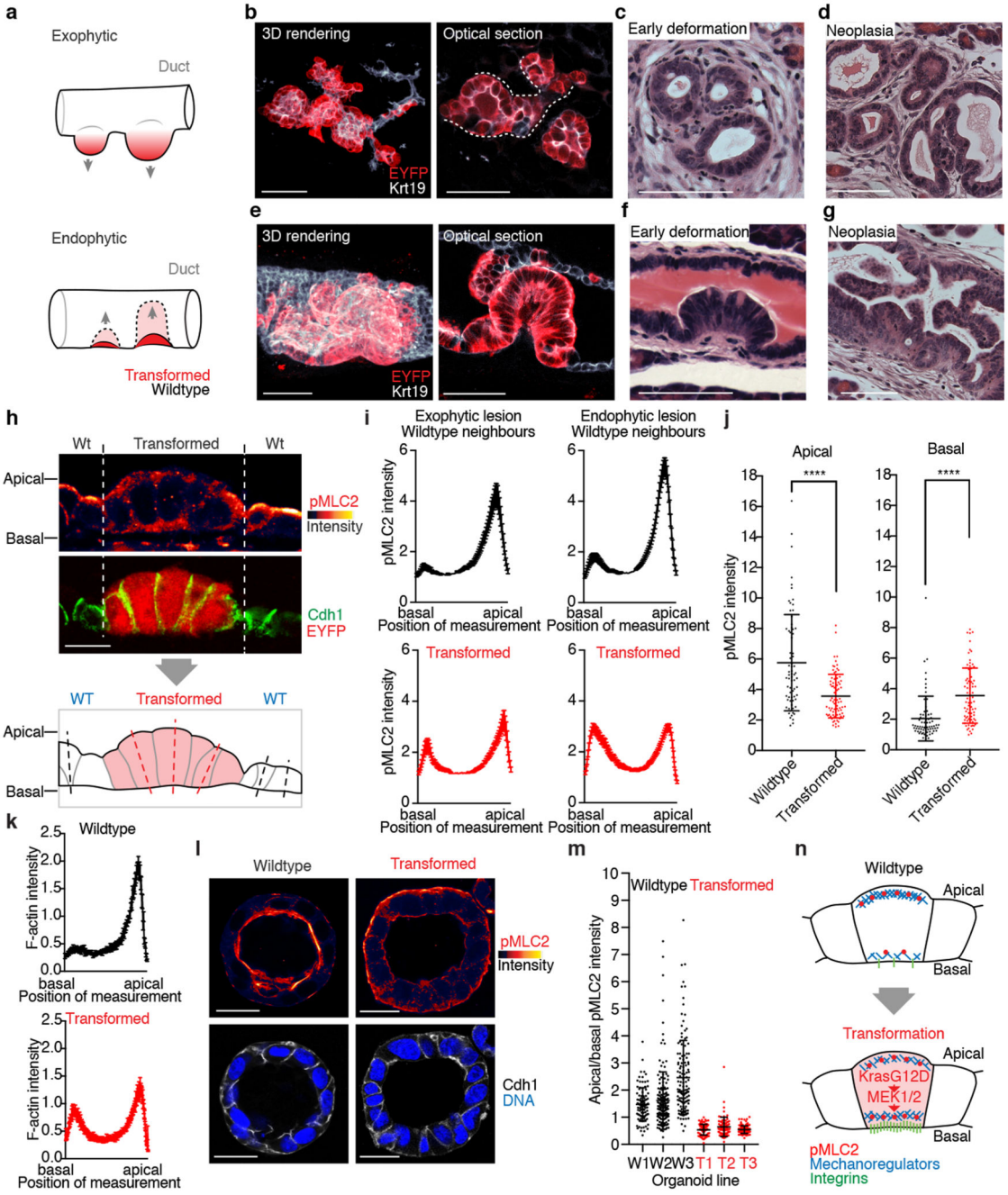

Fig. 2. Heterogeneity of neoplasia induction in the pancreatic ducts.

a, Exophytic and endophytic ductal deformations. **b-g**, FLASH comparison with 2D histology. **b**, **e**, 3D view (left) and optical section (right) of KFCk19 exophytic (**b**) and endophytic (**e**) deformations 10 days post-recombination; n=3 mice. **c**, **d**, **f**, **g**, H&E staining of exophytic (**c**, **d**) and endophytic (**f**, **g**) lesions 10 days (**c**, **f**) and 21 days (**d**, **g**) post-recombination. 10 days, n=4 mice; 21 days, n=5 mice. **h**, pMLC2, Cdh1 and EYFP staining of a transformed, but undeformed KFCk19 clone and position of pixel intensity measurement (dotted lines). Cdh1 demarcates lateral cell surfaces. n=7 mice. **i**, Basal-apical

pMLC2 pixel intensity profiles measured as in (**h**). Mean ± s.e.m. (exophytic: n=45 transformed, n=35 wildtype cells; endophytic: n=79 transformed, n=71 wildtype cells from 7 mice). **j**, Basal and apical pMLC2 intensities (maxima of cell profiles from endophytic lesions); n=71 wildtype, n=79 transformed cells from 7 mice. Mean ± s.d., ****P <0.0001 (two-sided Mann-Whitney test). **k**, Basal-apical F-actin intensity profiles of cells from KPC mice or wildtype littermates, measured as in (h). Mean ± s.e.m. (wildtype, n=120 cells from 4 mice; transformed, n=212 cells from 3 mice). **l**, pMLC2 and Cdh1 staining of pancreatic wildtype and transformed (KPC) organoids. Apical cell surfaces face inward. n=3 wildtype and 3 KPC organoid lines. **m**, Apical-basal pMLC2 intensities of single cells from KPC organoids (T1 to T3) or wildtype organoids (W1 to W3). Mean ± s.d. (W1, n=95 cells; W2, n=166 cells; W3, n=131 cells; T1, n=88 cells; T2, n=80 cells; T3, n=118 cells). **n**, Summary of mechanical changes in transformed cells. Scale bars, 50 μm (**b**, **e**), 100 μm (**c**, **d**, **f**, **g**), 10 μm (**h**), 20 μm. (**l**).

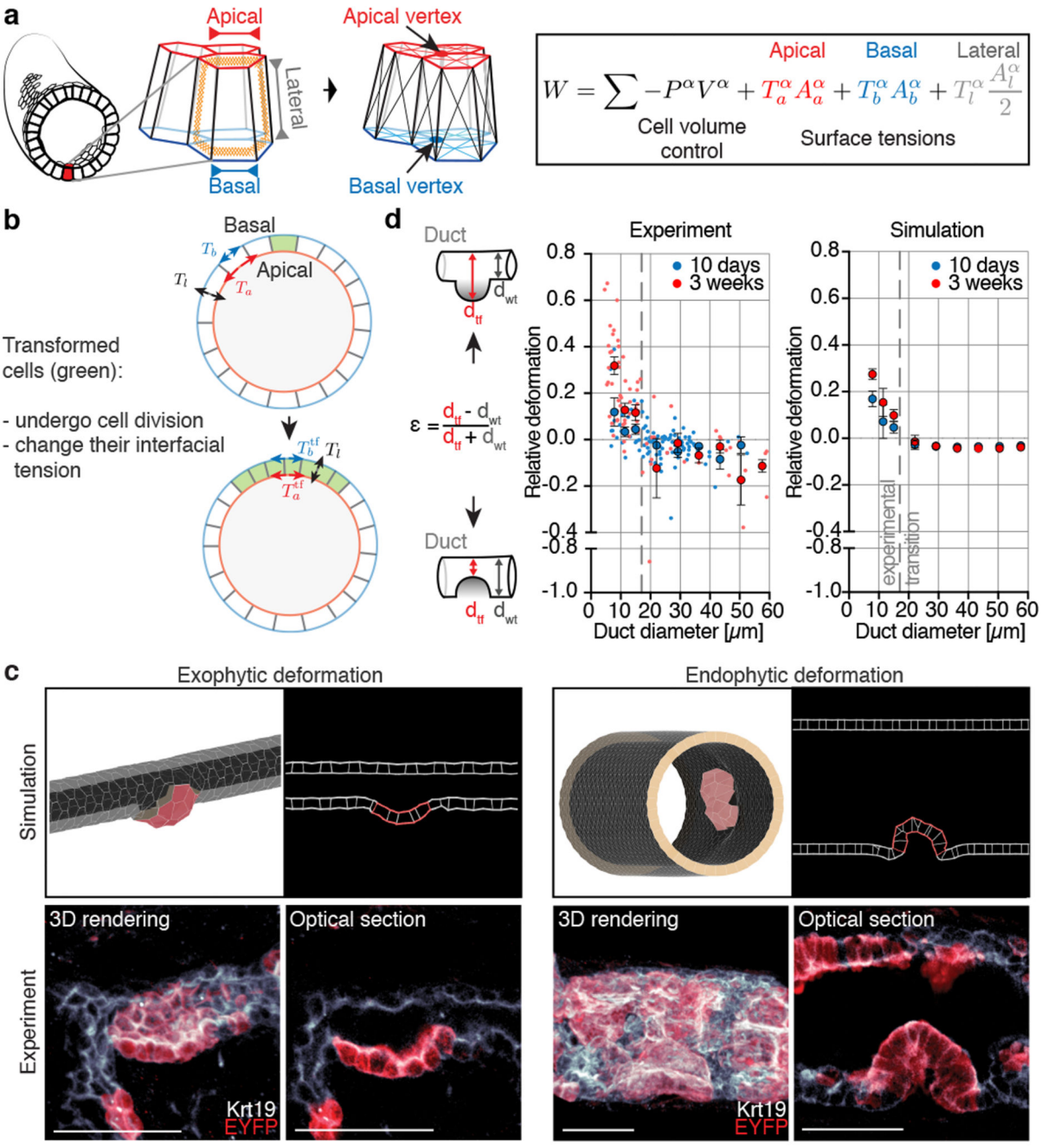

Fig. 3. Duct diameter instruction of lesion morphology.

a, Schematic of the 3D vertex model. Apical and basal vertices represent tissue geometry. Effective energy W, taking into account intracellular hydrostatic pressure P_a constraining cell volume V^{α}, with apical, basal and lateral surface tensions T_a^{α}, T_b^{α} and T_l^{α}, is minimised to obtain mechanically equilibrated shapes. A_a^{α}, A_b^{α} and A_l^{α} denote apical, basal and lateral surface areas. **b**, For wildtype duct simulations, pMLC2 intensity and cell aspect ratio measurements determine mechanical parameters (see Supplementary Modelling

Europe PMC Funders Author Manuscripts

Europe PMC Funders Author Manuscripts

Procedures). A single transformed cell then undergoes cycles of cell division. Cellular interfacial tension changes are introduced in simulated transformed cells in line with pMLC2 intensity changes (Fig. 2j). **c**, Representation of simulated deformed ducts with diameters below 17 μm (exophytic deformation) and above 17 μm (endophytic deformation) and comparison with experimental data from KFCk19 mice. n=7 mice. Scale bars, 50 μm. **d**, Quantification of ductal deformation of the pancreas ductal tree as a function of duct diameter. Relative deformation defined by $(d_{tf} - d_{wt})/(d_{tf} + d_{wt})$, with d_{tf} and d_{wt} the apical to apical ductal diameter within and outside the lesion respectively. Positive deformation indicates an evaginating (exophytic) lesion, negative deformation an invaginating (endophytic) lesion. In both simulations and experiments, a transition from exophytic to endophytic lesions occurs at ~17 μm. Left, Experimental measurements (smaller dots) and binned mean ± s.e.m. (larger dots) (10 days, n=112 ducts from 3 mice; 3 weeks, n=88 ducts from 4 mice). Gray dotted line demarcates transition through 0 as estimated in Extended Fig. 8d. Right, Predicted ductal deformation as function of duct diameter, from vertex model simulations. Dots are mean ± s.e.m., n=10 simulations.

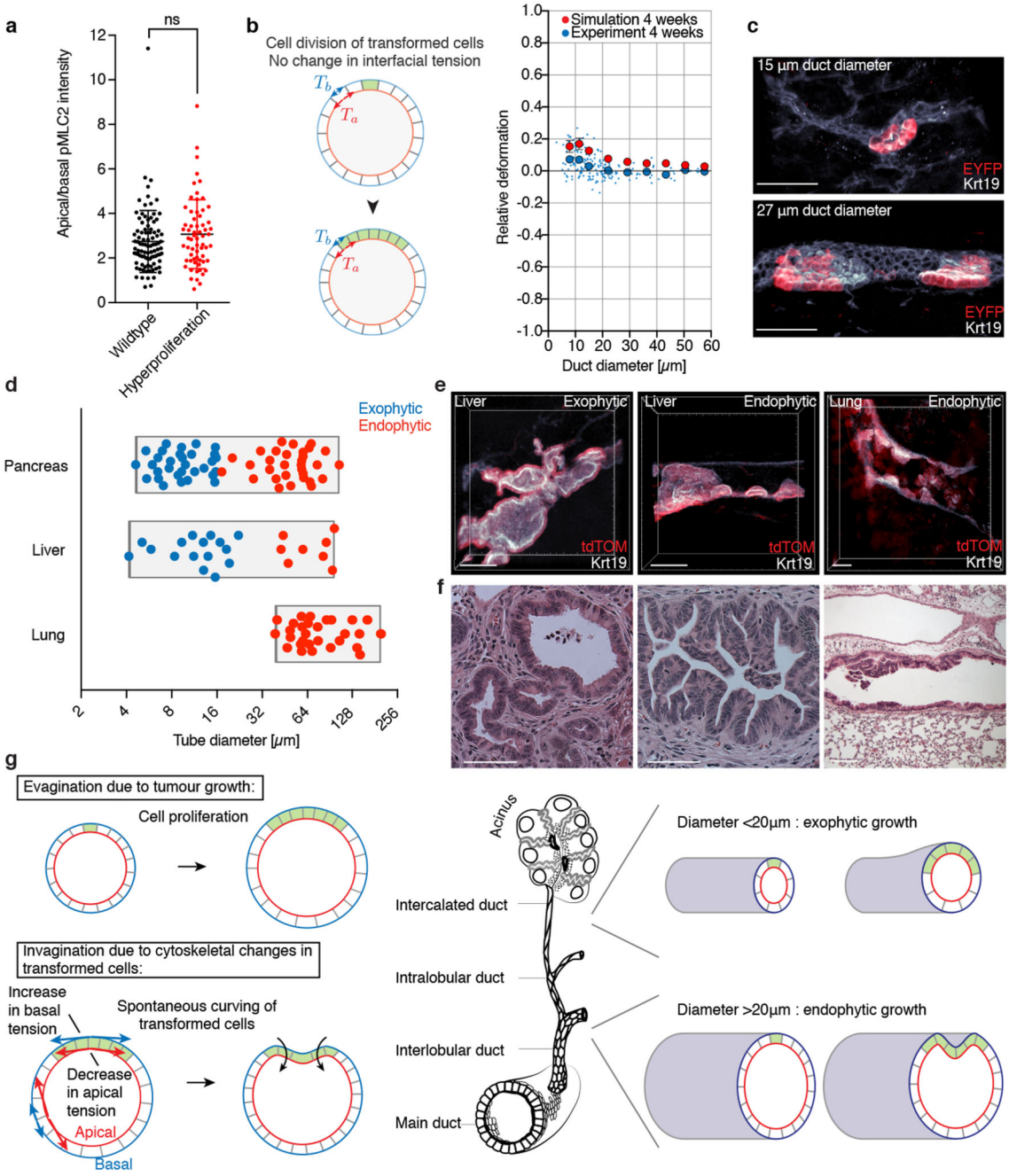

Fig. 4. Lesion morphology dependence on tension imbalance and tissue curvature.

a, Quantification of pMLC2 distribution in recombined (hyperproliferative) cells and wildtype neighbours from FCk19 mice; n=93 wildtype cells, n=64 hyperproliferative cells from 6 mice. Mean ± s.d., ns – not significant P=0.1712 (two-sided Mann-Whitney test). **b**, Measured (small blue dots), binned experimental (large blue dots, mean ± s.e.m.), and simulated (large red dots, mean ± s.e.m.) ductal deformations of hyperproliferating ducts with mechanical parameters as in wildtype cells of Fig. 3d. Measurements from n=216 FCk19 clones from 4 mice. Hyperproliferation simulated by selecting one duct cell and

Europe PMC Funders Author Manuscripts

performing cell divisions until a clone of 21 cells is formed; n=10 simulations. **c**, 3D view of small and large ducts with local hyperproliferative cell patches (red). n=4 mice. **d**, Distribution of endophytic and exophytic neoplasia in KFCk19 pancreatic ducts (n=62 lesions from 6 mice), intrahepatic biliary tree (n=24 lesions from 3 mice) and bronchiolar system (n=29 lesions from 3 mice), as a function of tube diameter outside the lesion. **e**, FLASH stainings for Krt19 and tdTomato on liver (n=3) and lung (n=3). **f**, H&E stainings of tissue sections through endophytic and exophytic lesions from liver (n=3) and lung (n=3). **g**, Model of ductal transformation into exophytic and endophytic neoplastic lesions. Scale bars, 50 μm (**c**), 100 μm (**e**, **f**).

Europe PMC Funders Author Manuscripts